

# ON A NOVEL FULLY DECOUPLED, SECOND-ORDER ACCURATE ENERGY STABLE NUMERICAL SCHEME FOR A BINARY FLUID-SURFACTANT PHASE-FIELD MODEL\*

XIAOFENG YANG<sup>†</sup>

**Abstract.** The binary fluid surfactant phase-field model, coupled with two Cahn–Hilliard equations and Navier–Stokes equations, is a very complex nonlinear system, which poses many challenges to the design of numerical schemes. As far as the author knows, due to the highly nonlinear coupling nature, there is no fully decoupled scheme with second-order accuracy in time for numerical approximation. This paper proposes a novel decoupling approach by introducing a nonlocal auxiliary variable and its associated ODE to deal with the nonlinear coupling terms that satisfy the so-called *zero-energy-contribution* property. By combining it with other proven effective methods (the projection method of the Navier–Stokes equations and the SAV method of linearizing nonlinear potential), we arrive at a fully decoupled, linear, unconditionally energy stable scheme with second-order time accuracy. At each time step, only a few fully decoupled linear elliptic equations with constant coefficients are needed to be solved, which shows the advantages of ease of implementation and efficiency. We also prove the unconditional energy stability rigorously and provide various numerical simulations in two and three dimensions to demonstrate its stability and accuracy, numerically.

**Key words.** fully decoupled, second-order, phase-field, unconditional energy stability, fluid-surfactant, Navier–Stokes

**AMS subject classifications.** 65N12, 65M12, 65M70

**DOI.** 10.1137/20M1336734

**1. Introduction.** In this paper, we focus on the numerical approximation of the phase-field model of a binary fluid surfactant system, which includes the nonlinear coupling of two Cahn–Hilliard equations and Navier–Stokes equations. The use of the phase-field method to simulate the fluid surfactant system can be traced back to the pioneering work of Laradji and co-authors in [29, 30] around two decades ago, as well as many subsequent modeling/analysis/simulation works in [8, 9, 14, 20, 26, 28, 37, 41, 53, 55, 56, 57, 58, 69], etc. For the binary phase-field surfactant model, two phase-field variables are usually used to represent the local concentration difference of the two fluids and the local surfactant concentration, respectively. Some physical properties are included in the total free energy, including hydrophilicity-hydrophobicity interaction and the phenomenon of high concentration of surfactants at the liquid interface. By using the gradient flow method to minimize the total energy, a partial model containing two coupled nonlinear Cahn–Hilliard equations can be obtained. Moreover, if the fluid properties of two substances are considered, the full model needs to further couple the Navier–Stokes equations by using the surface tension and advection terms.

Many successful attempts have been made for numerical simulations of various models of binary fluid surfactant systems. Regarding algorithm developments, however, compared with the partial model containing only two coupled Cahn–Hilliard equations, the full flow-coupled model has received less attention due to its highly cou-

---

\*Submitted to the journal’s Computational Methods in Science and Engineering section May 8, 2020; accepted for publication (in revised form) November 23, 2020; published electronically March 30, 2021.

<https://doi.org/10.1137/20M1336734>

**Funding:** This work was partially supported by the U.S. National Science Foundation under grant numbers DMS-1720212, DMS-1818783 and DMS-2012490.

<sup>†</sup>Department of Mathematics, University of South Carolina, Columbia, SC 29208 USA (xfyang@math.sc.edu).

pled nonlinear nature (cf. [27, 35, 61, 62, 71]). As we all know, for the two constituents of the full flow-coupled model, the Navier–Stokes equations, and the Cahn–Hilliard equation, there are many effective methods available for each individual equation, for example, the projection method [16, 17, 18, 19, 34, 39, 40, 49] for Navier–Stokes equations, the linear stabilization [48, 51, 67], convex splitting [7, 23, 43, 45, 68], quadratization (invariant energy quadratization (IEQ) [2, 60, 63, 64] and scalar auxiliary variable (SAV) [3, 47, 65]), nonlinear derivative [5], nonlinear quadrature [11, 12, 42] methods for phase-field models, etc. Therefore, one might consider that by simply applying the above methods to each component, an effective numerical method can be easily developed, especially a fully decoupled scheme with second-order time accuracy and unconditional energy stability; however, this is not the case.

So far, for the flow-coupled phase-field model, as far as the author knows, the only numerical scheme with a fully decoupled structure and maintaining energy stability was developed in [38, 50, 51], where the method to achieve complete decoupling is to add a stabilization term to the explicit advective velocity. However, this fully decoupled scheme in [38, 50, 51] is only first-order time-accurate, and it needs to solve the Cahn–Hilliard equation with variable coefficients. More importantly, it seems very difficult to upgrade the stabilization method to the second-order version. The main difficulty in establishing the second-order fully decoupled scheme is how to design a proper discretization method with second-order time accuracy to deal with the advection and surface tension terms, so that the computation of the phase-field equation can be decoupled from the momentum equation while maintaining the energy stability. Various attempts have been made in this direction, including the above-mentioned stabilization technique or explicit-implicit combination method [15, 21, 22, 23, 33, 49, 51, 63], etc. However, unfortunately, the ideal scheme has not been designed yet. More unfortunately, coupled nonlinear terms such as advection/surface tension exist in almost all flow-coupled phase-field models, which makes the development of a second-order fully decoupled scheme a universal difficulty.

Therefore, the main purpose of this paper is to overcome this challenge and develop a novel full decoupling approach that can also achieve the second-order time accuracy and unconditionally energy stability. To this end, we notice that advection and surface tension terms satisfy a so-called *zero-energy-contribution* feature. In other words, when deducing the energy law, after applying the inner products of some appropriate functions, the results of these terms will completely cancel out. Thus, using this property, we rewrite the PDE system by introducing a nonlocal variable and designing an ordinary differential equation (ODE) containing the inner products of the advection and surface tension with some specific functions. This ODE is trivial at the continuous level because all the terms contained in it are zero. But after discretization, it can help eliminate all the troublesome terms originated from those nonlinear coupled terms, thereby obtaining unconditional energy stability. Besides, the introduction of the nonlocal variable can decompose each discrete equation into multiple subequations that can be solved independently, thereby obtaining a fully decoupled structure.

By combining this novel decoupling method with the existing proven effective methods (including the projection method of the Navier–Stokes equations and the SAV method of linearizing the nonlinear energy potential), we finally arrive at an unconditionally energy stable, linear, fully decoupled, and second-order time-accurate scheme. The implementation of this scheme is very simple, and it only needs to solve a few linear independent equations with constant coefficients at each time step, which means that the computational cost is very low. We also give a rigorous proof of the

solvability and unconditional energy stability of the scheme and further simulate various numerical examples in two and three dimensions to demonstrate the stability and accuracy numerically. To the best of the author’s knowledge, the scheme developed in this article is the first to have all the desired characteristics (i.e., linear, fully decoupled, second-order accurate in time and unconditional energy stable) for solving the flow-coupled phase-field model. In addition, the decoupling method developed in this paper is universally applicable. First, it can be combined with other linear methods (such as the linear stabilization, IEQ, etc.) to form various types of fully decoupled and energy-stable schemes. Second, it can also be applied to any nonlinear coupling type model. As long as the coupling term follows the zero-energy-contribution property, this method is always applicable for generating an effective full decoupling scheme.

We organize the rest of this article in the following manner. We first briefly introduce the fluid surfactant model and derive its energy law structure in section 2. A second-order fully decoupled numerical scheme is constructed in section 3 and we further describe its implementations in detail. The unconditional energy stability is proved rigorously as well. Then various benchmark two-dimensional (2D) and 3D numerical simulations are shown in section 4, including the accuracy/stability tests, spinodal decomposition in two and three dimensions, and droplets coalescence/nonmergence phenomena with and without surfactant application under shear flow in two and three dimensions. In section 5, some concluding remarks are given.

**2. Model and its energy law.** Now, we briefly introduce the representative binary fluid-surfactant flow-coupled model proposed in [35, 57, 58, 69]. Suppose  $\Omega \in \mathbb{R}^d$  with  $d = 2, 3$  is a smooth, open, bounded, connected domain, the two functions  $\phi(\mathbf{x}, t)$  and  $\rho(\mathbf{x}, t)$  are used to simulate the dynamics in a binary fluid-surfactant systems, where  $\phi(\mathbf{x}, t)$  is used to represent the local concentration difference of the two fluids, namely,

$$(2.1) \quad \phi(\mathbf{x}, t) = \begin{cases} 1 & \text{fluid I,} \\ -1 & \text{fluid II,} \end{cases}$$

with a thin transition layer with width  $O(\epsilon)$  linking these two distinct values, and  $\rho(\mathbf{x}, t)$  is introduced to be the concentration of surfactants. The interface of the two-phase fluids is then described by the zero level set of  $\phi$ :  $\Gamma_t = \{\mathbf{x} : \phi(\mathbf{x}, t) = 0\}$ .

The total free energy that couples the two variables  $\phi, \rho$  is postulated as follows:

$$(2.2) \quad \begin{aligned} E(\phi, \rho, \mathbf{u}) &= \int_{\Omega} \left( \frac{1}{2} |\mathbf{u}|^2 + \lambda_1 \left( \frac{1}{2} |\nabla \phi|^2 + \frac{1}{\epsilon^2} F(\phi) \right) + \lambda_2 \left( \frac{\gamma}{2} |\nabla \rho|^2 + \frac{1}{\eta^2} G(\rho) \right) + W(\phi, \rho) \right) d\mathbf{x}, \end{aligned}$$

where  $\mathbf{u}$  is the average fluid velocity field, the three nonlinear potentials  $F(\phi), G(\rho)$ , and  $W(\phi, \rho)$  are given by

$$(2.3) \quad \begin{cases} F(\phi) = \frac{1}{4}(\phi^2 - 1)^2, & W(\phi, \rho) = -\frac{\theta}{2}\rho|\nabla\phi|^2 - \alpha\rho\phi + \frac{\zeta}{4}|\nabla\phi|^4, \\ G(\rho) = \begin{cases} \rho \ln \rho + (1 - \rho) \ln \sigma + G_r(\sigma, \rho) & \text{if } \rho \geq 1 - \sigma, \\ \rho \ln \rho + (1 - \rho) \ln(1 - \rho) & \text{if } \sigma \leq \rho \leq 1 - \sigma, \\ (1 - \rho) \ln(1 - \rho) + \rho \ln \sigma + G_l(\sigma, \rho) & \text{if } \rho \leq \sigma, \end{cases} \end{cases}$$

and  $\lambda_1, \lambda_2, \epsilon, \gamma, \eta, \theta, \zeta, \alpha, \sigma$  are all positive parameters. It can be seen from the free

energy that for the variable  $\phi$ , the mixing potential introduced by this model takes into account the hydrophilicity (gradient)-hydrophobicity (double-well) of interactions. The bulk energy for the concentration variable  $\rho$  is given similarly but the nonlinear potential  $G(\rho)$  takes a different form, where  $\eta$  is a penalty parameter, and the two functions  $G_r(\sigma, \rho), G_l(\sigma, \rho)$  are used to extend the logarithmic potential (see Remark 2.1), where  $\sigma \ll 1$  is a preassigned parameter for extension (we set  $\sigma = 0.01$  in all simulations). All the couplings between the surfactants and fluid interface are contained in the nonlinear potential  $W(\phi, \rho)$ , where the  $\theta$  term controls the degree to which the surfactant affects the fluid-interface, the  $\zeta$  term can guarantee the total free energy bounded from below [69], and the asymmetric term related to  $\alpha$  indicates the different solubility of the surfactant in the two components of the fluid.

*Remark 2.1.* For the binary surfactant model, the choice of nonlinear potential  $G(\rho)$  has great flexibility. In the earliest work of the phase-field surfactant model [29],  $G(\phi)$  is chosen as the quadratic polynomial type. In [28, 37, 41],  $G(\phi)$  is selected as the fourth-order double-well potential type. In [57, 58, 69],  $G(\phi)$  is selected as the Flory–Huggins logarithmic type ( $\rho \ln \rho + (1 - \rho) \ln(1 - \rho)$ ), which is also used in this paper. However, the domain of the logarithmic potential is an open interval  $(0, 1)$ , so it must be strictly ensured that the value of the calculated solution is in this domain; otherwise, the calculation will easily overflow. Therefore, the usual practice is to modify the logarithmic potential to be an extended form defined on  $(-\infty, \infty)$ . The two functions  $G_r(\sigma, \rho), G_l(\sigma, \rho)$  given in (2.3) are used for the extension. Here, we extend the Flory–Huggins logarithmic potential to a  $C^2(-\infty, \infty)$  and convex function by setting  $G_l(\sigma, \rho) = \frac{\rho^4}{12\sigma^3} + \frac{2\rho}{3} - \frac{3\sigma}{4}$  and  $G_r(\sigma, \rho) = \frac{(1-\rho)^4}{12\sigma^3} + \frac{2(1-\rho)}{3} - \frac{3\sigma}{4}$ . This kind of extension helps to bound the coupling potential  $W(\phi, \rho)$  from below. Another type of  $C^2(-\infty, \infty)$ -extension for the logarithmic potential was given in [4, 6, 69].

Then, by using the Cahn–Hilliard type ( $H^{-1}$ -gradient flow) relaxation kinetics for  $\phi$  and  $\rho$  and assuming that the fluid is incompressible and follows the generalized Fick’s law, that is, the mass flux is proportional to the gradient of the chemical potential, we get the hydrodynamics coupled binary surfactant model, which reads as

$$(2.4) \quad \phi_t + \nabla \cdot (\mathbf{u}\phi) = M_1 \Delta \mu,$$

$$(2.5) \quad \mu = \frac{\delta E}{\delta \phi} = \lambda_1 \left( -\Delta \phi + \frac{1}{\epsilon^2} f(\phi) \right) + W_\phi,$$

$$(2.6) \quad \rho_t + \nabla \cdot (\mathbf{u}\rho) = M_2 \Delta \omega,$$

$$(2.7) \quad \omega = \frac{\delta E}{\delta \rho} = \lambda_2 \left( -\gamma \Delta \rho + \frac{1}{\eta^2} g(\rho) \right) + W_\rho,$$

$$(2.8) \quad \mathbf{u}_t + (\mathbf{u} \cdot \nabla) \mathbf{u} + \nabla p - \nu \Delta \mathbf{u} + \phi \nabla \mu + \rho \nabla \omega = 0,$$

$$(2.9) \quad \nabla \cdot \mathbf{u} = 0,$$

where

$$(2.10) \quad \begin{cases} W_\phi = \frac{\delta W(\phi, \rho)}{\delta \phi} = \theta \nabla \cdot (\rho \nabla \phi) + \alpha \rho - \zeta \nabla \cdot (|\nabla \phi|^2 \nabla \phi), \\ W_\rho = \frac{\delta W(\phi, \rho)}{\delta \rho} = -\frac{\theta}{2} |\nabla \phi|^2 - \alpha \phi, f(\phi) = F'(\phi) = \phi(\phi^2 - 1), g(\rho) = G'(\rho), \end{cases}$$

$M_1, M_2$  are two mobility parameters,  $\nu$  is the fluid viscosity,  $p$  is the pressure, the

nonlinear terms  $\nabla \cdot (\mathbf{u}\phi), \nabla \cdot (\mathbf{u}\rho), (\mathbf{u} \cdot \nabla)\mathbf{u}$  are advection, and the nonlinear terms  $\phi\nabla\mu$  and  $\rho\nabla\omega$  in the momentum (2.8) are the induced surface tensions.

In this paper, we consider the following two kinds of boundary conditions:

(2.11) (i) all variables are periodic or

(2.12) (ii)  $\mathbf{u}|_{\partial\Omega} = \mathbf{0}, \partial_{\mathbf{n}}\phi|_{\partial\Omega} = \partial_{\mathbf{n}}\rho|_{\partial\Omega} = \nabla\mu \cdot \mathbf{n}|_{\partial\Omega} = \nabla\omega \cdot \mathbf{n}|_{\partial\Omega} = 0,$

where  $\mathbf{n}$  is the unit outward normal on the boundary  $\partial\Omega$ . The initial conditions read as

(2.13)  $\mathbf{u}|_{(t=0)} = \mathbf{u}^0, p|_{(t=0)} = p^0, \phi|_{(t=0)} = \phi^0, \rho|_{(t=0)} = \rho^0.$

The PDE energy law of the system (2.4)–(2.9) can be obtained by the following process. For (2.4), we take the inner product with  $\mu$  in  $L^2$  and use integration by parts to get

(2.14) 
$$(\phi_t, \mu) = -M_1 \|\nabla\mu\|^2 - \underbrace{\int_{\Omega} \nabla \cdot (\mathbf{u}\phi)\mu dx}_I.$$

For (2.5), we take the inner product with  $-\phi_t$  in  $L^2$  to get

(2.15) 
$$-(\mu, \phi_t) = -\frac{d}{dt} \int_{\Omega} \lambda_1 \left( \frac{1}{2} |\nabla\phi|^2 + \frac{1}{\epsilon^2} F(\phi) \right) dx - \int_{\Omega} W_{\phi} \phi_t dx.$$

For (2.6), we take the inner product with  $\omega$  in  $L^2$  to obtain

(2.16) 
$$(\rho_t, \omega) = -M_2 \|\nabla\omega\|^2 - \underbrace{\int_{\Omega} \nabla \cdot (\mathbf{u}\rho)\omega dx}_{II}.$$

For (2.7), we take the inner product with  $-\rho_t$  in  $L^2$  to get

(2.17) 
$$-(\omega, \rho_t) = -\frac{d}{dt} \int_{\Omega} \lambda_2 \left( \frac{\gamma}{2} |\nabla\rho|^2 + \frac{1}{\eta^2} G(\rho) \right) dx - \int_{\Omega} W_{\rho} \rho_t dx.$$

For (2.8), after taking the inner product with  $\mathbf{u}$  in  $L^2$  and using (2.9) and integration by parts, we get

(2.18) 
$$\frac{d}{dt} \int_{\Omega} \frac{1}{2} |\mathbf{u}|^2 dx + \nu \|\nabla\mathbf{u}\|^2 = - \underbrace{\int_{\Omega} \phi \nabla\mu \cdot \mathbf{u} dx}_{III} - \underbrace{\int_{\Omega} \rho \nabla\omega \cdot \mathbf{u} dx}_{IV} - \underbrace{\int_{\Omega} (\mathbf{u} \cdot \nabla)\mathbf{u} \cdot \mathbf{u} dx}_{V}.$$

Combining the above five equations, the obtained energy law reads as follows:

(2.19) 
$$\frac{d}{dt} E(\mathbf{u}, \phi, \rho) = -M_1 \|\nabla\mu\|^2 - M_2 \|\nabla\omega\|^2 - \nu \|\nabla\mathbf{u}\|^2 \leq 0,$$

where the three negative terms at the right end specify the diffusion rate of the total free energy  $E(\mathbf{u}, \phi, \rho)$ .

*Remark 2.2.* We note that when deriving the PDE energy law (2.19), after using integration by parts and boundary conditions, I and III, II and IV are canceled,

respectively. The term  $V$  vanishes due to the divergence-free condition and boundary conditions as well. This means that the advection and surface tension terms do not contribute to the total free energy or energy diffusion rate. Therefore, the zero-energy-contribution property behind these terms provides some guidance for the development of decoupling type schemes, which will be given in the next section.

**3. Numerical scheme.** We aim to construct an effective time marching scheme to solve the system (2.4)–(2.9). We expect that the scheme can not only achieve full decoupling, linearity, and second-order accuracy but also maintain unconditional energy stability. To achieve this goal, the main difficulty lies in how to develop a decoupling approach to deal with the coupled nonlinear terms between the flow field and the phase-field variables. If we give up the full decoupling structure and only need a linear scheme with second-order accuracy in time and unconditional energy stability, the second-order IEQ or SAV method is a good choice (see [69, 71]). However, the simple application of these methods cannot achieve the fully decoupled structure we expect.

Therefore, in this paper, in order to achieve all the above goals, especially the full-decoupling, we develop a novel method whose key idea is to introduce a nonlocal auxiliary variable and design its associated ODE by using the well-known by often ignored zero-energy-contribution characteristics satisfied by those coupled nonlinear terms causing troubles. It helps to decompose all equations into several equations that can be solved independently, thus achieving the full-decoupling structure. The detailed process is as follows.

**3.1. Reformulation.** First, we introduce a nonlocal variable  $Q(t)$  and design a special ODE system that reads as

$$(3.1) \quad \begin{cases} Q_t = \int_{\Omega} \left( \nabla \cdot (\mathbf{u}\phi)\mu + (\phi\nabla\mu) \cdot \mathbf{u} + \nabla \cdot (\mathbf{u}\rho)\omega + (\rho\nabla\omega) \cdot \mathbf{u} + (\mathbf{u} \cdot \nabla)\mathbf{u} \cdot \mathbf{u} \right) d\mathbf{x}, \\ Q|_{(t=0)} = 1, \end{cases}$$

under the condition of  $\nabla \cdot \mathbf{u} = 0$  and the boundary conditions specified in (2.11). Utilizing the zero-energy-contribution property satisfied by the advection and surface tension terms (see Remark 2.2), it is easy to see that the ODE (3.2) is equivalent to

$$(3.2) \quad \begin{cases} Q_t = 0, \\ Q|_{(t=0)} = 1, \end{cases}$$

which means the exact solution of (3.1) is  $Q(t) = 1$ .

Second, we define a nonlocal variable  $U(t)$  such that

$$(3.3) \quad U(t) = \sqrt{\int_{\Omega} \left( \lambda_1 \frac{F(\phi)}{\epsilon^2} + \lambda_2 \frac{G(\rho)}{\eta^2} + W(\phi, \rho) \right) d\mathbf{x} + B},$$

where  $B$  is a constant to guarantee the radicand is always positive. We can always find such a constant  $B$  since the summation of the three terms in the radicand are always bounded from below (where the term associated with  $\alpha$  can be always bounded from below by  $F(\phi)$  and  $G(\rho)$ , and the term associated with  $\theta$  can be bounded by  $G(\rho)$  and the quartic gradient term associated with  $\zeta$ ; see also in [69]).

Then, by combining the two nonlocal variables  $Q$  and  $U$  and the trivial evolution (3.1), the system (2.4)–(2.9) is reformulated to the following form:

$$(3.4) \quad \phi_t + Q \nabla \cdot (\mathbf{u} \phi) = M_1 \Delta \mu,$$

$$(3.5) \quad \mu = -\lambda_1 \Delta \phi + HU,$$

$$(3.6) \quad \rho_t + Q \nabla \cdot (\mathbf{u} \rho) = M_2 \Delta \omega,$$

$$(3.7) \quad \omega = -\lambda_2 \gamma \Delta \rho + RU,$$

$$(3.8) \quad U_t = \frac{1}{2} \int_{\Omega} (H \phi_t + R \rho_t) d\mathbf{x},$$

$$(3.9) \quad \mathbf{u}_t + Q(\mathbf{u} \cdot \nabla) \mathbf{u} + \nabla p - \nu \Delta \mathbf{u} + Q \phi \nabla \mu + Q \rho \nabla \omega = 0,$$

$$(3.10) \quad \nabla \cdot \mathbf{u} = 0,$$

$$(3.11) \quad Q_t = \int_{\Omega} \left( \nabla \cdot (\mathbf{u} \phi) \mu + (\phi \nabla \mu) \cdot \mathbf{u} + \nabla \cdot (\mathbf{u} \rho) \omega + (\rho \nabla \omega) \cdot \mathbf{u} + (\mathbf{u} \cdot \nabla) \mathbf{u} \cdot \mathbf{u} \right) d\mathbf{x},$$

where

$$H(\phi) = \frac{\lambda_1 \frac{f(\phi)}{\epsilon^2} + W_{\phi}}{\sqrt{\int_{\Omega} \left( \lambda_1 \frac{F(\phi)}{\epsilon^2} + \lambda_2 \frac{G(\rho)}{\eta^2} + W(\phi, \rho) \right) d\mathbf{x} + B}},$$

$$R(\phi) = \frac{\lambda_2 \frac{g(\rho)}{\eta^2} + W_{\rho}}{\sqrt{\int_{\Omega} \left( \lambda_1 \frac{F(\phi)}{\epsilon^2} + \lambda_2 \frac{G(\rho)}{\eta^2} + W(\phi, \rho) \right) d\mathbf{x} + B}}.$$

We give some detailed descriptions of the reformulated system in the following remarks.

*Remark 3.1.* Some modifications have been made to the original system (2.4)–(2.9) to obtain the new system (3.4)–(3.11). First, we rewrite (2.5) and (2.7) with the new variables  $U$  and take the time derivative of  $U$  to obtain (3.8). Second, we simply add the ODE (3.1) into the obtained system. Note that under the divergence-free conditions and the boundary conditions of the system, (3.1) is equivalent to  $Q = 1$ . Hence, for the advection and surface tension terms satisfying the zero-energy-contribution feature, we multiply them with  $Q$ . Therefore, the new PDE system using the variables  $(\mathbf{u}, p, \phi, \rho, \mu, \omega, Q, U)$  is equivalent to the original PDE system (2.4)–(2.9) using the variables  $(\mathbf{u}, p, \phi, \rho, \mu, \omega)$ .

*Remark 3.2.* Using the nonlocal variable  $U$ , the complex form of the nonlinear terms in the chemical potentials turns to a very simple form ( $HU$  and  $RU$ ). This method is the so-called SAV method, which can linearize the nonlinear term very effectively (see [3, 46, 47, 52, 65, 71]). We also notice that in [71], the SAV method has been used to develop an energy stable scheme for the Cahn–Hilliard phase-field surfactant model without the flow field, that is, the case of  $\mathbf{u} \equiv \mathbf{0}$ . This paper considers the full flow-coupled model which includes more coupled nonlinear structures; therefore, the corresponding numerical scheme requires the participation of more effective techniques, especially the new decoupling method developed in this article.

The transformed system (3.4)–(3.11) satisfies the following initial conditions:

$$(3.12) \quad \begin{aligned} \mathbf{u}|_{(t=0)} &= \mathbf{u}^0, p|_{(t=0)} = p^0, \phi|_{(t=0)} = \phi^0, \rho|_{(t=0)} = \rho^0, \\ Q|_{(t=0)} &= 1, U|_{(t=0)} = \sqrt{\int_{\Omega} \left( \lambda_1 \frac{F(\phi^0)}{\epsilon^2} + \lambda_2 \frac{G(\rho^0)}{\eta^2} + W(\phi^0, \rho^0) \right) d\mathbf{x} + B}. \end{aligned}$$

Note that the new system (3.4)–(3.11) is equivalent to the original PDE system (2.4)–(2.9) because the summation of all nonlinear integrals on the right end of (3.11) are just zero, which means  $q \equiv 1$ . Meanwhile, the new transformed system (3.4)–(3.11) also follows an energy dissipative law which can be derived by performing a similar process as obtaining (2.19). We present the detailed process since the energy stability proof in the discrete level follows the same line.

We take the inner product of (3.4) by  $\mu$  in  $L^2$  and use integration by parts to obtain

$$(3.13) \quad (\phi_t, \mu) = -M_1 \|\nabla \mu\|^2 - \underbrace{Q \int_{\Omega} \nabla \cdot (\mathbf{u}\phi) \mu dx}_{\text{I}}.$$

By taking the inner product of (3.5) with  $-\phi_t$  in  $L^2$ , we get

$$(3.14) \quad -(\mu, \phi_t) = -\frac{d}{dt} \int_{\Omega} \frac{\lambda_1}{2} |\nabla \phi|^2 dx - U \int_{\Omega} H \phi_t dx.$$

Taking the inner product of (3.6) by  $\omega$  in  $L^2$ , we obtain

$$(3.15) \quad (\rho_t, \omega) = -M_2 \|\nabla \omega\|^2 - \underbrace{Q \int_{\Omega} \nabla \cdot (\mathbf{u}\rho) \omega dx}_{\text{II}}.$$

Taking the inner product of (3.7) with  $-\rho_t$  in  $L^2$ , we get

$$(3.16) \quad -(\omega, \rho_t) = -\frac{d}{dt} \int_{\Omega} \frac{\lambda_2 \gamma}{2} |\nabla \rho|^2 dx - U \int_{\Omega} R \rho_t dx.$$

By multiplying (3.8) with  $2U$ , we obtain

$$(3.17) \quad \frac{d}{dt} |U|^2 = U \int_{\Omega} (H \phi_t + R \rho_t) dx.$$

Taking the inner product of (3.9) with  $\mathbf{u}$  in  $L^2$  and using integration by parts and (2.9), we obtain

$$(3.18) \quad \frac{d}{dt} \int_{\Omega} \frac{1}{2} |\mathbf{u}|^2 dx + \nu \|\nabla \mathbf{u}\|^2 = \underbrace{-Q \int_{\Omega} \phi \nabla \mu \cdot \mathbf{u} dx}_{\text{III}} - \underbrace{Q \int_{\Omega} \rho \nabla \omega \cdot \mathbf{u} dx}_{\text{IV}} - \underbrace{Q \int_{\Omega} (\mathbf{u} \cdot \nabla) \mathbf{u} \cdot \mathbf{u} dx}_{\text{V}}.$$

By multiplying (3.11) with  $Q$ , we obtain

$$(3.19) \quad \begin{aligned} \frac{d}{dt} \left( \frac{1}{2} |Q|^2 \right) &= \underbrace{Q \int_{\Omega} \nabla \cdot (\mathbf{u}\phi) \mu dx}_{\text{I}_1} + \underbrace{Q \int_{\Omega} \nabla \cdot (\mathbf{u}\rho) \omega dx}_{\text{II}_1} + \underbrace{Q \int_{\Omega} \phi \nabla \mu \cdot \mathbf{u} dx}_{\text{III}_1} \\ &\quad + \underbrace{Q \int_{\Omega} \rho \nabla \omega \cdot \mathbf{u} dx}_{\text{IV}_1} + \underbrace{Q \int_{\Omega} (\mathbf{u} \cdot \nabla) \mathbf{u} \cdot \mathbf{u} dx}_{\text{V}_1}. \end{aligned}$$

Combining (3.13)–(3.19), the obtained energy law in the new form reads as

$$(3.20) \quad \frac{d}{dt} E(\mathbf{u}, \phi, \rho, Q, U) = -M_1 \|\nabla \mu\|^2 - M_2 \|\nabla \omega\|^2 - \nu \|\nabla \mathbf{u}\|^2,$$

where

(3.21)

$$E(\mathbf{u}, \phi, \rho, U, Q) = \int_{\Omega} \left( \frac{1}{2} |\mathbf{u}|^2 + \frac{\lambda_1}{2} |\nabla \phi|^2 + \frac{\lambda_2 \gamma}{2} |\nabla \rho|^2 \right) d\mathbf{x} + |U|^2 + \frac{1}{2} |Q|^2 - B.$$

*Remark 3.3.* The advantage of adding the simple ODE of  $Q$  to the system can be seen from the above process of energy law derivation. Taking the advection and surface tension terms related to  $\phi$  as an example, in the original formulation, the two nonlinear integrals I in (2.14) and III in (2.18) cancel each other out, so that these two terms must be discretized in the same way when designing the algorithm, which leads to a coupled type scheme of  $\phi$  and  $\mathbf{u}$ . But using the new formulation, term I in (3.13) will be offset by term  $I_1$  in (3.19). This allows greater flexibility when discretizing the two terms I and III because they no longer need to cancel each other out. Therefore, the introduction of the  $Q$  (3.19) makes it possible to design the fully decoupled scheme. A similar technique was used to handle the advection term when developing explicit-type numerical schemes for the Navier–Stokes equations (see [31, 32]).

**3.2. Numerical scheme.** We introduce some notation here. Let  $\delta t > 0$  be a time step size and set  $t^n = n\delta t$  for  $0 \leq n \leq N$  with  $T = N\delta t$ . The  $L^2$  inner product of any two functions  $\phi(\mathbf{x})$  and  $\psi(\mathbf{x})$  is denoted by  $(\phi(\mathbf{x}), \psi(\mathbf{x})) = \int_{\Omega} \phi(\mathbf{x})\psi(\mathbf{x})d\mathbf{x}$ , and the  $L^2$  norm of  $\phi(\mathbf{x})$  is denoted by  $\|\phi\|^2 = (\phi, \phi)$ . Let  $\psi^n$  be the numerical approximation to the function  $\psi(\cdot, t)|_{t=t^n}$ .

Now, we are ready to construct a numerical scheme to solve the model (3.4)–(3.11). After using the second-order backward differentiation formula (BDF2), a time marching scheme reads as follows.

We solve  $(\tilde{\mathbf{u}}, \mathbf{u}, \phi, \mu, \rho, \omega, U, Q)^{n+1}$  by

$$(3.22) \quad \frac{a\phi^{n+1} - b\phi^n + c\phi^{n-1}}{2\delta t} + Q^{n+1} \nabla \cdot (\mathbf{u}^* \phi^*) = M_1 \Delta \mu^{n+1},$$

$$(3.23) \quad \mu^{n+1} = -\lambda_1 \Delta \phi^{n+1} + \frac{S_1}{\epsilon^2} (\phi^{n+1} - \phi^*) + H^* U^{n+1},$$

$$(3.24) \quad \frac{a\rho^{n+1} - b\rho^n + c\rho^{n-1}}{2\delta t} + Q^{n+1} \nabla \cdot (\mathbf{u}^* \rho^*) = M_2 \Delta \omega^{n+1},$$

$$(3.25) \quad \omega^{n+1} = -\lambda_2 \gamma \Delta \rho^{n+1} + \frac{S_2}{\eta^2} (\rho^{n+1} - \rho^*) + R^* U^{n+1},$$

$$(3.26) \quad \begin{aligned} & aU^{n+1} - bU^n + cU^{n-1} \\ &= \frac{1}{2} \int_{\Omega} (H^*(a\phi^{n+1} - b\phi^n + c\phi^{n-1}) + R^*(a\rho^{n+1} - b\rho^n + c\rho^{n-1})) d\mathbf{x}, \end{aligned}$$

$$(3.27) \quad \begin{aligned} & \frac{a\tilde{\mathbf{u}}^{n+1} - b\mathbf{u}^n + c\mathbf{u}^{n-1}}{2\delta t} - \mathbf{u}^n \\ &+ Q^{n+1} (\mathbf{u}^* \cdot \nabla) \mathbf{u}^* + \nabla p^n - \nu \Delta \tilde{\mathbf{u}}^{n+1} + Q^{n+1} \phi^* \nabla \mu^* + Q^{n+1} \rho^* \nabla \omega^* = 0, \end{aligned}$$

$$(3.28) \quad \begin{aligned} & \frac{aQ^{n+1} - bQ^n + cQ^{n-1}}{2\delta t} \\ &= \int_{\Omega} \left( \nabla \cdot (\mathbf{u}^* \phi^*) \mu^{n+1} + (\phi^* \nabla \mu^*) \cdot \tilde{\mathbf{u}}^{n+1} + \nabla \cdot (\mathbf{u}^* \rho^*) \omega^{n+1} \right. \\ & \quad \left. + (\rho^* \nabla \omega^*) \cdot \tilde{\mathbf{u}}^{n+1} + (\mathbf{u}^* \cdot \nabla) \mathbf{u}^* \cdot \tilde{\mathbf{u}}^{n+1} \right) d\mathbf{x}, \end{aligned}$$

and

$$(3.29) \quad \frac{a}{2\delta t}(\mathbf{u}^{n+1} - \tilde{\mathbf{u}}^{n+1}) + \nabla(p^{n+1} - p^n) = 0,$$

$$(3.30) \quad \nabla \cdot \mathbf{u}^{n+1} = 0,$$

where

$$(3.31) \quad \begin{cases} a = 3, b = 4, c = 1, \mathbf{u}^* = 2\mathbf{u}^n - \mathbf{u}^{n-1}, \phi^* = 2\phi^n - \phi^{n-1}, \rho^* = 2\rho^n - \rho^{n-1}, \\ \mu^* = 2\mu^n - \mu^{n-1}, \omega^* = 2\omega^n - \omega^{n-1}, H^* = H(\phi^*, \rho^*), R^* = R(\phi^*, \rho^*), \end{cases}$$

and  $S_1$  and  $S_2$  are two prespecified stability parameters.

The boundary conditions for the unknown variables  $(\mathbf{u}, \tilde{\mathbf{u}}, \phi, \rho, \mu, \omega, p)^{n+1}$  are either periodic or

$$(3.32)$$

$$\tilde{\mathbf{u}}^{n+1}|_{\partial\Omega} = \mathbf{0}, \mathbf{u}^{n+1} \cdot \mathbf{n}|_{\partial\Omega} = \partial_{\mathbf{n}}\phi^{n+1}|_{\partial\Omega} = \partial_{\mathbf{n}}\rho^{n+1}|_{\partial\Omega} = \partial_{\mathbf{n}}\mu^{n+1}|_{\partial\Omega} = \partial_{\mathbf{n}}\omega^{n+1}|_{\partial\Omega} = 0.$$

*Remark 3.4.* The initialization of the second-order scheme requires the values of all variables at  $t = t^1$ , which can be obtained by constructing a first-order scheme using the backward Euler method. In the above second-order scheme (3.22)–(3.30), as long as we set  $a = 2, b = 2, c = 0, \psi^* = \psi^0$  for any variable  $\psi$ , the first-order scheme can be easily obtained.

*Remark 3.5.* The second-order projection type (pressure-correction) method is used in the developed scheme to solve the Navier–Stokes equation. This method effectively decouples the computations of pressure from that of the velocity field. To obtain the pressure, we just apply the divergence operator to (3.29) and then obtain the following Poisson equation for  $p^{n+1}$ , i.e.,

$$(3.33) \quad -\Delta p^{n+1} = -\frac{a}{2\delta t} \nabla \cdot \tilde{\mathbf{u}}^{n+1} - \Delta p^n.$$

Once  $p^{n+1}$  is computed from (3.33), we update  $\mathbf{u}^{n+1}$  by using (3.29), i.e.,

$$(3.34) \quad \mathbf{u}^{n+1} = \tilde{\mathbf{u}}^{n+1} - \frac{2\delta t}{a} \nabla(p^{n+1} - p^n).$$

*Remark 3.6.* In the two Cahn–Hilliard equations of  $\phi$  and  $\rho$ , we add two second-order linear stabilization terms related to  $S_i, i = 1, 2$  in (3.23) and (3.25) to improve energy stability. Similar treatment had been used to apply the IEQ/SAV method for various gradient flow models (see [52, 69, 70]). Numerical experiments in section 4 (Figures 1, 3, 4) show that these two stabilizers can effectively improve energy stability when large time steps are used. Moreover, although these two additional stabilizers increase the splitting errors, the increased error is comparable to the error caused by the extrapolation to the nonlinear terms  $f(\phi)$  and  $g(\rho)$ .

**3.3. Implementation process.** However, it seems that the developed scheme (3.22)–(3.30) is not a fully decoupled scheme. All unknown variables are coupled together nonlocally. If we solve it using any direct iterative method, the time consumption can be considerable. Therefore, we develop the following process to eliminate all nonlocal terms and obtain a fully decoupled implementation.

First, we use the nonlocal scalar variable  $Q^{n+1}$  to split  $(\phi, \rho, \mu, \omega, U)^{n+1}$  into a linear combination that reads as

$$(3.35) \quad \begin{cases} \phi^{n+1} = \phi_1^{n+1} + Q^{n+1}\phi_2^{n+1}, \\ \rho^{n+1} = \rho_1^{n+1} + Q^{n+1}\rho_2^{n+1}, \\ \mu^{n+1} = \mu_1^{n+1} + Q^{n+1}\mu_2^{n+1}, \\ \omega^{n+1} = \omega_1^{n+1} + Q^{n+1}\omega_2^{n+1}, \\ U^{n+1} = U_1^{n+1} + Q^{n+1}U_2^{n+1}. \end{cases}$$

Then the scheme (3.22)–(3.25) can be rewritten as

$$(3.36) \quad \begin{cases} \frac{a}{2M_1\delta t}(\phi_1^{n+1} + Q^{n+1}\phi_2^{n+1}) + \frac{1}{M_1}Q^{n+1}\nabla \cdot (\mathbf{u}^* \phi^*) \\ \quad = \Delta(\mu_1^{n+1} + Q^{n+1}\mu_2^{n+1}) + \frac{1}{2M_1\delta t}(b\phi^n - c\phi^{n-1}), \\ \mu_1^{n+1} + Q^{n+1}\mu_2^{n+1} \\ \quad = \left(-\lambda_1\Delta + \frac{S_1}{\epsilon^2}\right)(\phi_1^{n+1} + Q^{n+1}\phi_2^{n+1}) + H^*(U_1^{n+1} + Q^{n+1}U_2^{n+1}) - \frac{S_1}{\epsilon^2}\phi^*, \\ \frac{a}{2M_2\delta t}(\rho_1^{n+1} + Q^{n+1}\rho_2^{n+1}) + \frac{1}{M_2}Q^{n+1}\nabla \cdot (\mathbf{u}^* \rho^*) \\ \quad = \Delta(\omega_1^{n+1} + Q^{n+1}\omega_2^{n+1}) + \frac{1}{2M_2\delta t}(b\rho^n - c\rho^{n-1}), \\ \omega_1^{n+1} + Q^{n+1}\omega_2^{n+1} \\ \quad = \left(-\lambda_2\Delta + \frac{S_2}{\eta^2}\right)(\rho_1^{n+1} + Q^{n+1}\rho_2^{n+1}) + R^*(U_1^{n+1} + Q^{n+1}U_2^{n+1}) - \frac{S_2}{\eta^2}\rho^*. \end{cases}$$

According to  $Q^{n+1}$ , the linear system (3.36) can be decomposed into two subsystems as follows,

$$(3.37) \quad \begin{cases} \frac{a}{2M_1\delta t}\phi_1^{n+1} = \Delta\mu_1^{n+1} + A_1, \\ \mu_1^{n+1} = \left(-\lambda_1\Delta + \frac{S_1}{\epsilon^2}\right)\phi_1^{n+1} + H^*U_1^{n+1} + B_1, \\ \frac{a}{2M_2\delta t}\rho_1^{n+1} = \Delta\omega_1^{n+1} + C_1, \\ \omega_1^{n+1} = \left(-\lambda_2\Delta + \frac{S_2}{\eta^2}\right)\rho_1^{n+1} + R^*U_1^{n+1} + D_1. \end{cases}$$

$$(3.38) \quad \begin{cases} \frac{a}{2M_1\delta t}\phi_2^{n+1} = \Delta\mu_2^{n+1} + A_2, \\ \mu_2^{n+1} = \left(-\lambda_1\Delta + \frac{S_1}{\epsilon^2}\right)\phi_2^{n+1} + H^*U_2^{n+1} + B_2, \\ \frac{a}{2M_2\delta t}\rho_2^{n+1} = \Delta\omega_2^{n+1} + C_2, \\ \omega_2^{n+1} = \left(-\lambda_2\Delta + \frac{S_2}{\eta^2}\right)\rho_2^{n+1} + R^*U_2^{n+1} + D_2, \end{cases}$$

where  $A_i, B_i, C_i, D_i, i = 1, 2$  are explicit, that read as

$$A_1 = \frac{1}{2M_1\delta t}(b\phi^n - c\phi^{n-1}), B_1 = -\frac{S_1}{\epsilon^2}\phi^*, C_1 = \frac{1}{2M_2\delta t}(b\rho^n - c\rho^{n-1}), D_1 = -\frac{S_2}{\eta^2}\rho^*,$$

$$A_2 = -\frac{1}{M_1}\nabla \cdot (\mathbf{u}^*\phi^*), B_2 = 0, C_2 = -\frac{1}{M_2}\nabla \cdot (\mathbf{u}^*\rho^*), D_2 = 0.$$

Note that the two subsystems (3.37) and (3.38) have the same form, so we only need to introduce a method to solve any one of them, and the other follows the same rule. Hence, we take the first subsystem (3.37) as an example. To solve (3.37), we continue to use the split technique, that is, the variables  $(\phi_1, \rho_1, \mu_1, \omega_1)^{n+1}$  are split into a linear combination form by the variable  $U_1^{n+1}$ , which read as

$$(3.39) \quad \begin{cases} \phi_1^{n+1} = \phi_{11}^{n+1} + U_1^{n+1}\phi_{12}^{n+1}, & \rho_1^{n+1} = \rho_{11}^{n+1} + U_1^{n+1}\rho_{12}^{n+1}, \\ \mu_1^{n+1} = \mu_{11}^{n+1} + U_1^{n+1}\mu_{12}^{n+1}, & \omega_1^{n+1} = \omega_{11}^{n+1} + U_1^{n+1}\omega_{12}^{n+1}. \end{cases}$$

By substituting the split form of all variables in (3.39) into (3.37) and decomposing the results according to  $U_1^{n+1}$ , we obtain four independent subsystems that read as

$$(3.40) \quad \begin{cases} \frac{a}{2M_1\delta t}\phi_{11}^{n+1} = \Delta\mu_{11}^{n+1} + A_1, \\ \mu_{11}^{n+1} = \left(-\lambda_1\Delta + \frac{S_1}{\epsilon^2}\right)\phi_{11}^{n+1} + B_1, \end{cases}$$

$$(3.41) \quad \begin{cases} \frac{a}{2M_1\delta t}\phi_{12}^{n+1} = \Delta\mu_{12}^{n+1}, \\ \mu_{12}^{n+1} = \left(-\lambda_1\Delta + \frac{S_1}{\epsilon^2}\right)\phi_{12}^{n+1} + H^*, \end{cases}$$

$$(3.42) \quad \begin{cases} \frac{a}{2M_2\delta t}\rho_{11}^{n+1} = \Delta\omega_{11}^{n+1} + C_1, \\ \omega_{11}^{n+1} = \left(-\lambda_2\Delta + \frac{S_2}{\eta^2}\right)\rho_{11}^{n+1} + D_1, \end{cases}$$

$$(3.43) \quad \begin{cases} \frac{a}{2M_2\delta t}\rho_{12}^{n+1} = \Delta\omega_{12}^{n+1}, \\ \omega_{12}^{n+1} = \left(-\lambda_2\Delta + \frac{S_2}{\eta^2}\right)\rho_{12}^{n+1} + R^*. \end{cases}$$

The boundary conditions for (3.40)–(3.43) are either periodic or

$$(3.44) \quad \begin{aligned} \partial_n\phi_{11}^{n+1}|_{\partial\Omega} &= \partial_n\phi_{12}^{n+1}|_{\partial\Omega} = \partial_n\rho_{11}^{n+1}|_{\partial\Omega} = \partial_n\rho_{12}^{n+1}|_{\partial\Omega} = 0, \\ \partial_n\mu_{11}^{n+1}|_{\partial\Omega} &= \partial_n\mu_{12}^{n+1}|_{\partial\Omega} = \partial_n\omega_{11}^{n+1}|_{\partial\Omega} = \partial_n\omega_{12}^{n+1}|_{\partial\Omega} = 0. \end{aligned}$$

One can easily solve  $(\phi_{11}, \phi_{12}, \rho_{11}, \rho_{12}, \mu_{11}, \mu_{12}, \omega_{11}, \omega_{12})^{n+1}$  from the above four subsystems (3.40)–(3.43) since all nonlinear terms are given explicitly.

We continue to solve (3.38) in a similar way where the variable  $U_2^{n+1}$  is used to split  $(\phi_2, \rho_2, \mu_2, \omega_2)^{n+1}$  into a linear combination, i.e.,

$$(3.45) \quad \begin{cases} \phi_2^{n+1} = \phi_{21}^{n+1} + U_2^{n+1}\phi_{22}^{n+1}, & \rho_2^{n+1} = \rho_{21}^{n+1} + U_2^{n+1}\rho_{22}^{n+1}, \\ \mu_2^{n+1} = \mu_{21}^{n+1} + U_2^{n+1}\mu_{22}^{n+1}, & \omega_2^{n+1} = \omega_{21}^{n+1} + U_2^{n+1}\omega_{22}^{n+1}. \end{cases}$$

Then the unknowns  $(\phi_{21}, \phi_{22}, \rho_{21}, \rho_{22}, \mu_{21}, \mu_{22}, \omega_{21}, \omega_{22})^{n+1}$  can be obtained by solving another four subsystems that are similar to (3.40)–(3.43) with the same boundary conditions as (3.44).

Second, we rewrite (3.26) in the following form:

$$(3.46) \quad U^{n+1} = \frac{1}{2} \int_{\Omega} (H^* \phi^{n+1} + R^* \rho^{n+1}) d\mathbf{x} + g^n,$$

where  $g^n = \frac{1}{a}(bU^n - cU^{n-1}) - \frac{1}{2a} \int_{\Omega} (H^*(b\phi^n - c\phi^{n-1}) + R^*(b\rho^n - c\rho^{n-1})) d\mathbf{x}$  is an explicit form. Substituting the linear form of  $(U, \phi, \rho)^{n+1}$  represented by  $Q^{n+1}$  given in (3.35) into (3.46), we get

$$(3.47) \quad U_1^{n+1} + Q^{n+1}U_2^{n+1} = \frac{1}{2} \int_{\Omega} \left( H^*(\phi_1^{n+1} + Q^{n+1}\phi_2^{n+1}) + R^*(\rho_1^{n+1} + Q^{n+1}\rho_2^{n+1}) \right) d\mathbf{x} + g^n.$$

Then, according to  $Q^{n+1}$ , we decompose (3.47) into the following two equalities:

$$(3.48) \quad \begin{cases} U_1^{n+1} = \frac{1}{2} \int_{\Omega} \left( H^* \phi_1^{n+1} + R^* \rho_1^{n+1} \right) d\mathbf{x} + g^n, \\ U_2^{n+1} = \frac{1}{2} \int_{\Omega} \left( H^* \phi_2^{n+1} + R^* \rho_2^{n+1} \right) d\mathbf{x}. \end{cases}$$

Substituting the linear form of  $(\phi_1, \rho_1, \phi_2, \rho_2)^{n+1}$  represented by  $U_1^{n+1}$  given in (3.39) into (3.48), we get

$$(3.49) \quad \begin{cases} U_1^{n+1} = \frac{1}{2} \int_{\Omega} \left( H^*(\phi_{11}^{n+1} + U_1^{n+1}\phi_{12}^{n+1}) + R^*(\rho_{11}^{n+1} + U_1^{n+1}\rho_{12}^{n+1}) \right) d\mathbf{x} + g^n, \\ U_2^{n+1} = \frac{1}{2} \int_{\Omega} \left( H^*(\phi_{21}^{n+1} + U_2^{n+1}\phi_{22}^{n+1}) + R^*(\rho_{21}^{n+1} + U_2^{n+1}\rho_{22}^{n+1}) \right) d\mathbf{x}. \end{cases}$$

After applying a simple factorization to (3.49), we derive

$$(3.50) \quad U_1^{n+1} = \frac{\frac{1}{2} \int_{\Omega} (H^* \phi_{11}^{n+1} + R^* \rho_{11}^{n+1}) d\mathbf{x} + g^n}{1 - \frac{1}{2} \int_{\Omega} H^* \phi_{12}^{n+1} d\mathbf{x} - \frac{1}{2} \int_{\Omega} R^* \rho_{12}^{n+1} d\mathbf{x}},$$

$$(3.51) \quad U_2^{n+1} = \frac{\frac{1}{2} \int_{\Omega} (H^* \phi_{21}^{n+1} + R^* \rho_{21}^{n+1}) d\mathbf{x}}{1 - \frac{1}{2} \int_{\Omega} H^* \phi_{22}^{n+1} d\mathbf{x} - \frac{1}{2} \int_{\Omega} R^* \rho_{22}^{n+1} d\mathbf{x}}.$$

We need to verify that  $U_1^{n+1}$  and  $U_2^{n+1}$  are solvable. This can be obtained by applying a simple energy estimate to the two subsystems (3.41) and (3.43). We take the  $L^2$  inner product of the first equation in (3.41) with  $-\mu_{12}$ , and of the second equation in (3.41) with  $\frac{a}{2M_1\delta t}\phi_{12}$ , and we derive

$$(3.52) \quad -\frac{a}{2M_1\delta t} \int_{\Omega} H^* \phi_{12}^{n+1} d\mathbf{x} = \|\nabla \mu_{12}^{n+1}\|^2 + \frac{a\lambda_1}{2M_1\delta t} \|\nabla \phi_{12}^{n+1}\|^2 + \frac{aS_1}{2\epsilon^2 M_1\delta t} \|\phi_{12}^{n+1}\|^2 \geq 0.$$

By implementing a similar process as in (3.43), we derive

$$(3.53) \quad -\frac{a}{2M_2\delta t} \int_{\Omega} R^* \rho_{12}^{n+1} d\mathbf{x} = \|\nabla \omega_{12}^{n+1}\|^2 + \frac{a\lambda_2}{2M_2\delta t} \|\nabla \rho_{12}^{n+1}\|^2 + \frac{aS_2}{2\eta^2 M_2\delta t} \|\rho_{12}^{n+1}\|^2 \geq 0.$$

Hence, the denominator in (3.50) is nonzero, which means that  $U_1^{n+1}$  is always solvable. Similarly,  $U_2^{n+1}$  can be always solved from (3.51) as well. After calculating  $U_1^{n+1}$  and  $U_2^{n+1}$ , we further obtain  $\phi_1^{n+1}, \rho_1^{n+1}, \mu_1^{n+1}, \omega_1^{n+1}$  from (3.39) and  $\phi_2^{n+1}, \rho_2^{n+1}, \mu_2^{n+1}, \omega_2^{n+1}$  from (3.45).

Third, for the velocity field  $\tilde{\mathbf{u}}^{n+1}, \mathbf{u}^{n+1}$  and the pressure  $p^{n+1}$  in the scheme (3.27) and (3.29)–(3.30), we also use the nonlocal variable  $Q^{n+1}$  to split them into the following linear combinations:

$$(3.54) \quad \tilde{\mathbf{u}}^{n+1} = \tilde{\mathbf{u}}_1^{n+1} + Q^{n+1}\tilde{\mathbf{u}}_2^{n+1}, \mathbf{u}^{n+1} = \mathbf{u}_1^{n+1} + Q^{n+1}\mathbf{u}_2^{n+1}, p^{n+1} = p_1^{n+1} + Q^{n+1}p_2^{n+1}.$$

By replacing these variables  $(\tilde{\mathbf{u}}, \mathbf{u}, p)^{n+1}$  in the scheme (3.27) and (3.29)–(3.30), and then splitting the obtained equations according to  $Q^{n+1}$ , we arrive at a system that includes two subequations. More precisely, from (3.27), the two split variables  $\tilde{\mathbf{u}}_i^{n+1}, i = 1, 2$ , follow the equations

$$(3.55) \quad \begin{cases} \frac{a}{2\delta t} \tilde{\mathbf{u}}_1^{n+1} - \nu \Delta \tilde{\mathbf{u}}_1^{n+1} = \sigma_1, \\ \frac{a}{2\delta t} \tilde{\mathbf{u}}_2^{n+1} - \nu \Delta \tilde{\mathbf{u}}_2^{n+1} = \sigma_2, \end{cases}$$

where  $\sigma_1, \sigma_2$  are explicit forms that are given by

$$(3.56) \quad \sigma_1 = -\nabla p^n + \frac{b\mathbf{u}^n - c\mathbf{u}^{n-1}}{2\delta t}, \sigma_2 = -(\mathbf{u}^* \cdot \nabla)\mathbf{u}^* - \phi^* \nabla \mu^* - \rho^* \nabla \omega^*.$$

Similarly, from (3.29)–(3.30), the two split variables  $\mathbf{u}_i^{n+1}, p_i^{n+1}, i = 1, 2$ , follow the equations

$$(3.57) \quad \begin{cases} \frac{3}{2\delta t}(\mathbf{u}_1^{n+1} - \tilde{\mathbf{u}}_1^{n+1}) + \nabla p_1^{n+1} = \nabla p^n, & \nabla \cdot \mathbf{u}_1^{n+1} = 0, \\ \frac{3}{2\delta t}(\mathbf{u}_2^{n+1} - \tilde{\mathbf{u}}_2^{n+1}) + \nabla p_2^{n+1} = 0, & \nabla \cdot \mathbf{u}_2^{n+1} = 0. \end{cases}$$

We request the four split variables  $\tilde{\mathbf{u}}_i^{n+1}, \mathbf{u}_i^{n+1}, i = 1, 2$ , follow the boundary conditions described in (3.32), i.e, they are either periodic or satisfy

$$(3.58) \quad \tilde{\mathbf{u}}_i^{n+1}|_{\partial\Omega} = \mathbf{0}, \mathbf{u}_i^{n+1} \cdot \mathbf{n}|_{\partial\Omega} = 0.$$

Fourth, we solve the auxiliary variable  $Q^{n+1}$ . Using the split form for the variables  $\mu^{n+1}, \omega^{n+1}, \tilde{\mathbf{u}}^{n+1}$ , one can rewrite (3.28) in the form

$$(3.59) \quad \left(\frac{a}{2\delta t} - \vartheta_2\right) Q^{n+1} = \frac{1}{2\delta t}(bQ^n - cQ^{n-1}) + \vartheta_1,$$

where  $\vartheta_i$  are all known from previous steps:

$$(3.60) \quad \vartheta_i = \int_{\Omega} \left( \nabla \cdot (\mathbf{u}^* \phi^*) \mu_i^{n+1} + (\phi^* \nabla \mu^*) \cdot \tilde{\mathbf{u}}_i^{n+1} + \nabla \cdot (\mathbf{u}^* \rho^*) \omega_i^{n+1} + (\rho^* \nabla \omega^*) \cdot \tilde{\mathbf{u}}_i^{n+1} + (\mathbf{u}^* \cdot \nabla)\mathbf{u}^* \cdot \tilde{\mathbf{u}}_i^{n+1} \right) d\mathbf{x}, i = 1, 2.$$

We verify that (3.59) is solvable by showing  $\frac{a}{2\delta t} - \vartheta_2 \neq 0$ . By taking the  $L^2$  inner product of the second equation in (3.55) with  $\tilde{\mathbf{u}}_2^{n+1}$ , we get

$$(3.61) \quad - \int_{\Omega} \left( (\phi^* \nabla \mu^*) \cdot \tilde{\mathbf{u}}_2^{n+1} + (\rho^* \nabla \omega^*) \cdot \tilde{\mathbf{u}}_2^{n+1} + (\mathbf{u}^* \cdot \nabla)\mathbf{u}^* \cdot \tilde{\mathbf{u}}_2^{n+1} \right) d\mathbf{x} = \frac{a}{2\delta t} \|\tilde{\mathbf{u}}_2^{n+1}\|^2 + \nu \|\nabla \tilde{\mathbf{u}}_2^{n+1}\|^2 \geq 0.$$

By taking the  $L^2$  inner product of the first equation in (3.38) with  $M_1\mu_2^{n+1}$ , of the second equation with  $-\frac{a}{2\delta t}\phi_2^{n+1}$ , of the third equation with  $M_2\omega_2^{n+1}$ , and of the fourth equation with  $-\frac{a}{2\delta t}\phi_2^{n+1}$ , and combining the obtained four equalities, we get

$$\begin{aligned}
 & - \int_{\Omega} (\nabla \cdot (\mathbf{u}^* \phi^*) \mu_2^{n+1} + \nabla \cdot (\mathbf{u}^* \rho^*) \omega_2^{n+1}) dx \\
 (3.62) \quad & = M_1 \|\nabla \mu_2^{n+1}\|^2 + M_2 \|\nabla \omega_2^{n+1}\|^2 + \frac{a\lambda_1}{2\delta t} \|\nabla \phi_2^{n+1}\|^2 + \frac{a\lambda_2}{2\delta t} \|\nabla \rho_2^{n+1}\|^2 \\
 & \quad + \frac{aS_1}{2\delta t \epsilon^2} \|\phi_2^{n+1}\|^2 + \frac{aS_2}{2\delta t \eta^2} \|\rho_2^{n+1}\|^2 + \frac{a}{2\delta t} U_2^{n+1} \int_{\Omega} (H^* \phi_2^{n+1} + R^* \rho_2^{n+1}) dx.
 \end{aligned}$$

From the second equation in (3.48), we derive  $U_2^{n+1} \int_{\Omega} (H^* \phi_2^{n+1} + R^* \rho_2^{n+1}) dx = \frac{1}{2}(U_2^{n+1})^2 \geq 0$ . Therefore, from (3.61) and (3.62), we derive  $-\vartheta_2 \geq 0$  that implies (3.59) is solvable.

Finally, we update  $(\phi, \rho, \mu, \omega, U)^{n+1}$  from (3.35) and  $(\tilde{\mathbf{u}}, \mathbf{u}, p)^{n+1}$  from (3.54).

In summary, we implement the scheme (3.22)–(3.30) in the following way:

- *Step 1:* Compute  $(\phi_{ij}, \rho_{ij}, \mu_{ij}, \omega_{ij})^{n+1}, i, j = 1, 2$ , from (3.40)–(3.43) and another similar four equations split from (3.38) using the variable  $U_2^{n+1}$ .
- *Step 2:* Update  $(U_1, U_2)^{n+1}$  from (3.50) and (3.51).
- *Step 3:* Update  $(\phi_i, \rho_i, \mu_i, \omega_i)^{n+1}, i = 1, 2$ , from (3.39) and (3.45).
- *Step 4:* Compute  $\tilde{\mathbf{u}}_i^{n+1}, i = 1, 2$ , from (3.55).
- *Step 5:* Compute  $\mathbf{u}_i^{n+1}$  and  $p_i^{n+1}, i = 1, 2$ , from (3.57).
- *Step 6:* Compute  $Q^{n+1}$  from (3.59).
- *Step 7:* Update  $(\phi, \rho, \mu, \omega, U)^{n+1}$  from (3.35), and  $(\tilde{\mathbf{u}}, \mathbf{u}, p)^{n+1}$  from (3.54).

Hence, the total computational cost needed by the scheme (3.22)–(3.30) at each time step includes solving eight independent elliptic linear systems in Step 1, two Poisson-type equations in Step 4, and two more Poisson type equations in Step 5. All these equations have constant coefficients and are fully decoupled, which means very efficient calculations in practice.

**3.4. Unconditional energy stability.** Now we prove that the scheme (3.22)–(3.30) is unconditionally energy stable as follows.

**THEOREM 3.1.** *The time-discrete scheme (3.22)–(3.30) satisfies the discrete energy dissipation law as follows:*

$$(3.63) \quad \frac{1}{\delta t} (E^{n+1} - E^n) \leq -\nu \|\nabla \tilde{\mathbf{u}}^{n+1}\|^2 - M_1 \|\nabla \mu^{n+1}\|^2 - M_2 \|\nabla \omega^{n+1}\|^2 \leq 0,$$

where

$$\begin{aligned}
 (3.64) \quad & E^{n+1} \\
 & = \frac{1}{2} \left( \frac{1}{2} \|\mathbf{u}^{n+1}\|^2 + \frac{1}{2} \|2\mathbf{u}^{n+1} - \mathbf{u}^n\|^2 \right) + \frac{\lambda_1}{2} \left( \frac{1}{2} \|\nabla \phi^{n+1}\|^2 + \frac{1}{2} \|2\nabla \phi^{n+1} - \nabla \phi^n\|^2 \right) \\
 & \quad + \frac{\lambda_2 \gamma}{2} \left( \frac{1}{2} \|\nabla \rho^{n+1}\|^2 + \frac{1}{2} \|2\nabla \rho^{n+1} - \nabla \rho^n\|^2 \right) + \left( \frac{1}{2} |U^{n+1}|^2 + \frac{1}{2} |2U^{n+1} - U^n|^2 \right) \\
 & \quad + \frac{1}{2} \left( \frac{1}{2} |Q^{n+1}|^2 + \frac{1}{2} |2Q^{n+1} - Q^n|^2 \right) + \frac{\delta t^2}{3} \|\nabla p^{n+1}\|^2 \\
 & \quad + \frac{S_1}{2\epsilon^2} \|\phi^{n+1} - \phi^n\|^2 + \frac{S_2}{2\eta^2} \|\rho^{n+1} - \rho^n\|^2.
 \end{aligned}$$

*Proof.* By taking the inner product of (3.27) with  $2\delta t \tilde{\mathbf{u}}^{n+1}$  in the  $L^2$  space, we obtain

$$\begin{aligned}
 (3.65) \quad & (3\tilde{\mathbf{u}}^{n+1} - 4\mathbf{u}^n + \mathbf{u}^{n-1}, \tilde{\mathbf{u}}^{n+1}) + 2\nu\delta t \|\nabla \tilde{\mathbf{u}}^{n+1}\|^2 + 2\delta t (\nabla p^n, \tilde{\mathbf{u}}^{n+1}) \\
 & + 2\delta t Q^{n+1} \int_{\Omega} (\mathbf{u}^* \cdot \nabla) \mathbf{u}^* \cdot \tilde{\mathbf{u}}^{n+1} d\mathbf{x} + 2\delta t Q^{n+1} \int_{\Omega} \phi^* \nabla \mu^* \cdot \tilde{\mathbf{u}}^{n+1} d\mathbf{x} \\
 & + 2\delta t Q^{n+1} \int_{\Omega} \rho^* \nabla \omega^* \cdot \tilde{\mathbf{u}}^{n+1} d\mathbf{x} = 0.
 \end{aligned}$$

From (3.29), for any variable  $\mathbf{v}$  with  $\nabla \cdot \mathbf{v} = 0$  and  $\mathbf{v} \cdot \mathbf{n}|_{\partial\Omega} = 0$ , we have

$$(3.66) \quad (\mathbf{u}^{n+1}, \mathbf{v}) = (\tilde{\mathbf{u}}^{n+1}, \mathbf{v}).$$

We derive the equality

$$\begin{aligned}
 (3.67) \quad & (3\tilde{\mathbf{u}}^{n+1} - 4\mathbf{u}^n + \mathbf{u}^{n-1}, \tilde{\mathbf{u}}^{n+1}) \\
 & = (3\tilde{\mathbf{u}}^{n+1} - 4\mathbf{u}^n + \mathbf{u}^{n-1}, \mathbf{u}^{n+1}) + (3\tilde{\mathbf{u}}^{n+1} - 4\mathbf{u}^n + \mathbf{u}^{n-1}, \tilde{\mathbf{u}}^{n+1} - \mathbf{u}^{n+1}) \\
 & = (3\mathbf{u}^{n+1} - 4\mathbf{u}^n + \mathbf{u}^{n-1}, \mathbf{u}^{n+1}) + (3\tilde{\mathbf{u}}^{n+1}, \tilde{\mathbf{u}}^{n+1} - \mathbf{u}^{n+1}) \\
 & = (3\mathbf{u}^{n+1} - 4\mathbf{u}^n + \mathbf{u}^{n-1}, \mathbf{u}^{n+1}) + 3(\tilde{\mathbf{u}}^{n+1} - \mathbf{u}^{n+1}, \tilde{\mathbf{u}}^{n+1} + \mathbf{u}^{n+1}) \\
 & = \frac{1}{2} (\|\mathbf{u}^{n+1}\|^2 - \|\mathbf{u}^n\|^2 + \|2\mathbf{u}^{n+1} - \mathbf{u}^n\|^2 - \|2\mathbf{u}^n - \mathbf{u}^{n-1}\|^2 \\
 & \quad + \|\mathbf{u}^{n+1} - 2\mathbf{u}^n + \mathbf{u}^{n-1}\|^2) + 3(\|\tilde{\mathbf{u}}^{n+1}\|^2 - \|\mathbf{u}^{n+1}\|^2),
 \end{aligned}$$

where we use the following identity:

$$(3.68) \quad 2(3a - 4b + c, a) = a^2 - b^2 + (2a - b)^2 - (2b - c)^2 + (a - 2b + c)^2.$$

We reformulate the projection step (3.29) as

$$(3.69) \quad \frac{3}{2\delta t} \mathbf{u}^{n+1} + \nabla p^{n+1} = \frac{3}{2\delta t} \tilde{\mathbf{u}}^{n+1} + \nabla p^n.$$

By taking the square of both sides of the above equation, we get

$$(3.70) \quad \frac{9}{4\delta t^2} \|\mathbf{u}^{n+1}\|^2 + \|\nabla p^{n+1}\|^2 = \frac{9}{4\delta t^2} \|\tilde{\mathbf{u}}^{n+1}\|^2 + \|\nabla p^n\|^2 + \frac{3}{\delta t} (\tilde{\mathbf{u}}^{n+1}, \nabla p^n).$$

Hence, by multiplying the above equation with  $2\delta t^2/3$ , we derive

$$(3.71) \quad \frac{3}{2} (\|\mathbf{u}^{n+1}\|^2 - \|\tilde{\mathbf{u}}^{n+1}\|^2) + \frac{2\delta t^2}{3} (\|\nabla p^{n+1}\|^2 - \|\nabla p^n\|^2) = 2\delta t (\tilde{\mathbf{u}}^{n+1}, \nabla p^n).$$

By taking the inner product of (3.29) with  $2\delta t \mathbf{u}^{n+1}$  in the  $L^2$  space, we have

$$(3.72) \quad \frac{3}{2} (\|\mathbf{u}^{n+1}\|^2 - \|\tilde{\mathbf{u}}^{n+1}\|^2 + \|\mathbf{u}^{n+1} - \tilde{\mathbf{u}}^{n+1}\|^2) = 0.$$

We combine (3.65), (3.67), (3.71), and (3.72) to obtain

$$\begin{aligned}
 (3.73) \quad & \frac{1}{2} (\|\mathbf{u}^{n+1}\|^2 - \|\mathbf{u}^n\|^2 + \|2\mathbf{u}^{n+1} - \mathbf{u}^n\|^2 - \|2\mathbf{u}^n - \mathbf{u}^{n-1}\|^2 + \|\mathbf{u}^{n+1} - 2\mathbf{u}^n + \mathbf{u}^{n-1}\|^2) \\
 & + \frac{3}{2} \|\mathbf{u}^{n+1} - \tilde{\mathbf{u}}^{n+1}\|^2 + \frac{2\delta t^2}{3} (\|\nabla p^{n+1}\|^2 - \|\nabla p^n\|^2) + 2\nu\delta t \|\nabla \tilde{\mathbf{u}}^{n+1}\|^2 \\
 & + 2\delta t Q^{n+1} \int_{\Omega} (\mathbf{u}^* \cdot \nabla) \mathbf{u}^* \cdot \tilde{\mathbf{u}}^{n+1} d\mathbf{x} + 2\delta t Q^{n+1} \int_{\Omega} \phi^* \nabla \mu^* \cdot \tilde{\mathbf{u}}^{n+1} d\mathbf{x} \\
 & + 2\delta t Q^{n+1} \int_{\Omega} \rho^* \nabla \omega^* \cdot \tilde{\mathbf{u}}^{n+1} d\mathbf{x} = 0.
 \end{aligned}$$

Computing the inner product of (3.22) with  $2\delta t\mu^{n+1}$  in the  $L^2$  space, we have

$$(3.74) \quad (3\phi^{n+1} - 4\phi^n + \phi^{n-1}, \mu^{n+1}) + 2\delta tQ^{n+1} \int_{\Omega} \nabla \cdot (\mathbf{u}^* \phi^*) \mu^{n+1} d\mathbf{x} + 2\delta tM_1 \|\nabla \mu^{n+1}\|^2 = 0.$$

Computing the  $L^2$  inner product of (3.23) with  $-(3\phi^{n+1} - 4\phi^n + \phi^{n-1})$ , we find

$$(3.75) \quad \mu^{n+1}, 3\phi^{n+1} - 4\phi^n + \phi^{n-1}) + \lambda_1(\nabla \phi^{n+1}, \nabla(3\phi^{n+1} - 4\phi^n + \phi^{n-1})) \\ + U^{n+1} \int_{\Omega} H^*(3\phi^{n+1} - 4\phi^n + \phi^{n-1}) d\mathbf{x} + \frac{S_1}{\epsilon^2}(\phi^{n+1} - \phi^*, 3\phi^{n+1} - 4\phi^n + \phi^{n-1}) = 0.$$

Computing the inner product of (3.24) with  $2\delta t\omega^{n+1}$  in the  $L^2$  space, we have

$$(3.76) \quad (3\rho^{n+1} - 4\rho^n + \rho^{n-1}, \omega^{n+1}) + 2\delta tQ^{n+1} \int_{\Omega} \nabla \cdot (\mathbf{u}^* \rho^*) \omega^{n+1} d\mathbf{x} + 2\delta tM_2 \|\nabla \omega^{n+1}\|^2 = 0.$$

Computing the  $L^2$  inner product of (3.25) with  $-(3\rho^{n+1} - 4\rho^n + \rho^{n-1})$ , we get

$$(3.77) \quad -(\omega^{n+1}, 3\rho^{n+1} - 4\rho^n + \rho^{n-1}) + \lambda_2(\nabla \rho^{n+1}, \nabla(3\rho^{n+1} - 4\rho^n + \rho^{n-1})) \\ + U^{n+1} \int_{\Omega} R^*(3\rho^{n+1} - 4\rho^n + \rho^{n-1}) d\mathbf{x} + \frac{S_2}{\eta^2}(\rho^{n+1} - \rho^*, 3\rho^{n+1} - 4\rho^n + \rho^{n-1}) = 0.$$

By multiplying (3.26) with  $2U^{n+1}$  and using (3.68), we obtain

$$(3.78) \quad |U^{n+1}|^2 - |U^n|^2 + |2U^{n+1} - U^n|^2 - |2U^n - U^{n-1}|^2 + |U^{n+1} - 2U^n + U^{n-1}|^2 \\ = U^{n+1} \int_{\Omega} (H^*(3\phi^{n+1} - 4\phi^n + \phi^{n-1}) + R^*(3\rho^{n+1} - 4\rho^n + \rho^{n-1})) d\mathbf{x}.$$

By multiplying (3.28) with  $2\delta tQ^{n+1}$  and using (3.68), we obtain

$$(3.79) \quad \frac{1}{2}(|Q^{n+1}|^2 - |Q^n|^2 + |2Q^{n+1} - Q^n|^2 - |2Q^n - Q^{n-1}|^2 + |Q^{n+1} - 2Q^n + Q^{n-1}|^2) \\ = 2\delta tQ^{n+1} \int_{\Omega} \nabla \cdot (\mathbf{u}^* \phi^*) \mu^{n+1} d\mathbf{x} \\ + 2\delta tQ^{n+1} \int_{\Omega} \phi^* \nabla \mu^* \cdot \tilde{\mathbf{u}}^{n+1} d\mathbf{x} + 2\delta tQ^{n+1} \int_{\Omega} \nabla \cdot (\mathbf{u}^* \rho^*) \omega^{n+1} d\mathbf{x} \\ + 2\delta tQ^{n+1} \int_{\Omega} \rho^* \nabla \omega^* \cdot \tilde{\mathbf{u}}^{n+1} d\mathbf{x} + 2\delta tQ^{n+1} \int_{\Omega} (\mathbf{u}^* \cdot \nabla) \mathbf{u}^* \cdot \tilde{\mathbf{u}}^{n+1} d\mathbf{x}.$$

Hence, by combining (3.73)–(3.79) and using (3.68), we arrive at

$$\begin{aligned}
(3.80) \quad & \frac{1}{2}(\|\mathbf{u}^{n+1}\|^2 - \|\mathbf{u}^n\|^2 + \|2\mathbf{u}^{n+1} - \mathbf{u}^n\|^2 - \|2\mathbf{u}^n - \mathbf{u}^{n-1}\|^2) + \frac{2\delta t^2}{3}(\|\nabla p^{n+1}\|^2 - \|\nabla p^n\|^2) \\
& + \frac{\lambda_1}{2}(\|\nabla\phi^{n+1}\|^2 - \|\nabla\phi^n\|^2 + \|\nabla(2\phi^{n+1} - \phi^n)\|^2 - \|\nabla(2\phi^n - \phi^{n-1})\|^2) \\
& + \frac{\lambda_2\gamma}{2}(\|\nabla\rho^{n+1}\|^2 - \|\nabla\rho^n\|^2 + \|\nabla(2\rho^{n+1} - \rho^n)\|^2 - \|\nabla(2\rho^n - \rho^{n-1})\|^2) \\
& + (|U^{n+1}|^2 - |U^n|^2 + |2U^{n+1} - U^n|^2 - |2U^n - U^{n-1}|^2) \\
& + \frac{1}{2}(|Q^{n+1}|^2 - |Q^n|^2 + |2Q^{n+1} - Q^n|^2 - |2Q^n - Q^{n-1}|^2) \\
& + \frac{S_1}{\epsilon^2}(\|\phi^{n+1} - \phi^n\|^2 - \|\phi^n - \phi^{n-1}\|^2) + \frac{S_2}{\eta^2}(\|\rho^{n+1} - \rho^n\|^2 - \|\rho^n - \rho^{n-1}\|^2) \\
& + \left\{ \frac{1}{2}\|\mathbf{u}^{n+1} - 2\mathbf{u}^n + \mathbf{u}^{n-1}\|^2 + \frac{3}{2}\|\mathbf{u}^{n+1} - \tilde{\mathbf{u}}^{n+1}\|^2 \right. \\
& \quad + \frac{\lambda_1}{2}\|\nabla(\phi^{n+1} - 2\phi^n + \phi^{n-1})\|^2 + \frac{\lambda_2\gamma}{2}\|\nabla(\rho^{n+1} - 2\rho^n + \rho^{n-1})\|^2 \\
& \quad + \frac{2S_1}{\epsilon^2}\|\phi^{n+1} - 2\phi^n + \phi^{n-1}\|^2 + \frac{2S_2}{\eta^2}\|\rho^{n+1} - 2\rho^n + \rho^{n-1}\|^2 \\
& \quad \left. + |U^{n+1} - 2U^n + U^{n-1}|^2 + \frac{1}{2}|Q^{n+1} - 2Q^n + Q^{n-1}|^2 \right\} \\
& = -2\delta t\nu\|\nabla\tilde{\mathbf{u}}^{n+1}\|^2 - 2\delta tM_1\|\nabla\mu^{n+1}\|^2 - 2\delta tM_2\|\nabla\omega^{n+1}\|^2,
\end{aligned}$$

where we use the following identity:

$$(3.81) \quad (3a - 4b + c)(a - 2b + c) = (a - b)^2 - (b - c)^2 + 2(a - 2b + c)^2.$$

Finally, from (3.80), we obtain (3.63) after dropping the positive terms in  $\{ \}$ .  $\square$

**4. Numerical simulations.** In this section, we first implement several numerical examples to verify the convergence and energy stability of the proposed scheme (3.22)–(3.30). Then, some benchmark simulations are proposed, including the spinodal decomposition in two and three dimensions and the droplets coalescence/nonmergence phenomena with and without surfactant application under shear flow in two and three dimensions, to demonstrate the effectiveness of the scheme.

In all the examples below, we set the computational domain to be a rectangular domain of  $[0, L_x] \times [0, L_y]$  or  $[0, L_x] \times [0, L_y] \times [0, L_z]$ . For the directions with periodic boundary conditions, we use the Fourier spectral method to discretize them. For the directions with physical boundary conditions specified in (3.32), the Legendre–Galerkin method is used to discretize them. The inf-sup stable pair  $(P_N, P_{N-2})$  is used for the velocity ( $\tilde{\mathbf{u}}$  and  $\mathbf{u}$ ) and pressure  $p$ , respectively, and  $P_N$  is used for the phase-field function  $\phi$  and  $\rho$ .

**4.1. Accuracy and stability test.** We first perform several convergence/stability tests to verify the accuracy and stability of the fully decoupled scheme using double auxiliary variables (3.22)–(3.30), referred to as DSAV. For comparisons, we also compute the numerical solutions by using the following schemes:

- DSAV scheme with  $Q$  but no  $S_i$  (to illustrate the effectiveness of the two stabilizers  $S_i, i = 1, 2$ ), i.e., the scheme (3.22)–(3.30) but with  $S_1 = S_2 = 0$ , referred to as SAV;

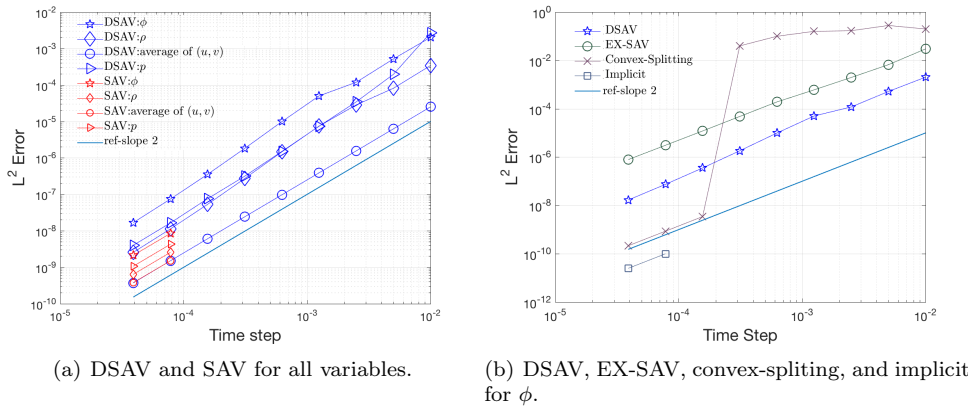


FIG. 1. Accuracy tests with the presumed exact solutions given in (4.1), where (a) the  $L^2$  numerical errors of  $\phi$ ,  $\rho$ , the average of  $\mathbf{u} = (u, v)$ ,  $p$ , are computed by DSAV (stabilized) and SAV (nonstabilized) with different time steps, and (b) the  $L^2$  numerical errors of  $\phi$  computed by DSAV, EX-SAV, convex-splitting, and implicit.

- DSAV scheme with  $S$  but no  $Q$  (by setting  $Q^k \equiv 1 \forall k$  such that (3.28) is removed), i.e., the advection and surface tension terms are all treated explicitly, referred to as EX-SAV;
- convex-splitting scheme (the nonlinear term  $f(\phi)$  is discretized using the second-order convex-splitting approach,  $g(\rho)$  is treated implicitly since  $G(\rho)$  is convex, and the advection/surface tension terms are treated by implicit-explicit combinations; see the similar scheme developed in [22, 23] for the Cahn–Hilliard/Navier–Stokes system for two-phase flows), referred to as convex-splitting;
- implicit scheme (all nonlinear terms are handled implicitly), referred to as implicit.

4.1.1. Presumed exact solution. We first perform the convergence tests by assuming the exact solution of the system (2.4)–(2.7) is given by the following formula:

$$(4.1) \quad \begin{cases} \phi(x, y, t) = \sin x \cos y \cos t, \rho(x, y, t) = (0.5 + 0.1 \sin x \cos y) \cos t, \\ \mathbf{u}(x, y, t) = (u(x, y, t), v(x, y, t)) = (\cos x \sin y, -\sin x \cos y) \cos t, \\ p(x, y, t) = \sin x \sin y \sin t. \end{cases}$$

We add some suitable force fields so that the solutions given in (4.1) can satisfy the system. The computational domain is  $\Omega = [0, 2\pi]^2$ , and the model parameters are set as

$$(4.2) \quad \begin{aligned} M_1 = M_2 = 1, \lambda_1 = \lambda_2 = 0.01, \epsilon = 0.08, \eta = 0.06, \\ \alpha = 2, \theta = 0.01, \zeta = 1e-5, \nu = 1, S_1 = S_2 = 0.1. \end{aligned}$$

The boundary conditions are set to periodic and  $129^2$  Fourier modes are used to discretize the space, so the discretization error in space is negligible compared to the time discretization error. In Figure 1(a) and (b), we plot the  $L^2$ -errors between the numerical solution and the exact solution at  $t = 0.2$  for unknown variables, where for all scenarios, the time step size ranges from  $\delta t = 0.01$  to  $\delta t = \frac{0.01}{2^8}$  with a factor of 1/2. In Figure 1(a), the  $L^2$  errors for all variables computed by DSAV and SAV

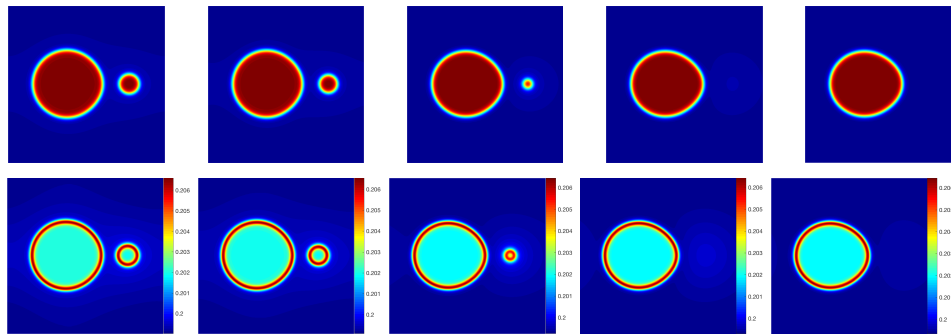


FIG. 2. The profiles of  $\phi$  and  $\rho$  computed by the scheme DSAV at  $t = 0.5, 0.72, 1.5, 1.75,$  and  $2$ , where the top row is  $\phi$  and the bottom row is  $\rho$ . The initial conditions are given in (4.3) and the time step is  $\delta t = 0.01/2^3$ .

are shown, and the scheme DSAV (with stabilizers) presents perfect second-order accuracy in time. Instead, for the scheme SAV (without stabilizers), when a large time step ( $\delta t > \frac{0.01}{2^7}$ ) is used, it blows up, thereby missing the corresponding error points. Only when using a smaller time step ( $\delta t \leq \frac{0.01}{2^7}$ ) can SAV display second-order accuracy.

In Figure 1(b), we compare the errors for  $\phi$  computed by DSAV, EX-SAV, convex-splitting, and implicit. The scheme EX-SAV also presents a second-order convergence rate. But for any fixed time step  $\delta t$ , the magnitude of the error computed using the scheme DSAV is smaller than that computed by EX-SAV. This means that the scheme DSAV is more accurate because the variable  $Q$  records all variances caused by the coupled nonlinear terms. For convex-splitting and implicit schemes, they present the second-order accuracy only when the adopted time step is small enough. For similar accuracy comparisons between different schemes for various phase-field models, we refer to [1, 10, 13, 25, 44, 54, 59].

**4.1.2. Mesh refinement in time.** We further test the convergence rate of the developed scheme DSAV by performing more mesh refinement tests in time. We still use the 2D domain of  $\Omega = [0, 2\pi]^2$  and assume the periodic boundary conditions. We discretize the space using  $129^2$  Fourier modes. The initial conditions of the two circles with different radii are as follows:

$$(4.3) \quad \begin{aligned} \phi^0(x, y) &= 1 + \sum_{i=1}^2 \tanh \left( \frac{r_i - \sqrt{(x - x_i)^2 + (y - y_i)^2}}{1.5\epsilon} \right), \\ \rho^0(x, y) &= 0.2, \mathbf{u}^0(x, y) = \mathbf{0}, p^0(x, y) = 0, \end{aligned}$$

where  $r_1 = 1.4, r_2 = 0.5, x_1 = \pi - 0.8, x_2 = \pi + 1.7, y_1 = y_2 = \pi$ . The model parameters are still from (4.2).

We first implement the scheme DSAV to the equilibrium state by using the time step size  $\delta t = \frac{0.01}{2^3}$ . Snapshots of the profiles of  $\phi$  and  $\rho$  at various times are shown in Figure 2, where we find that the coarsening effect is such that the small circle is absorbed into the large circle gradually. Meanwhile, we can see that concentration is high around the fluid interfaces due to the coupling between  $\phi$  and  $\rho$ , and the values of  $\rho$  are different in two bulk phases, which is due to the different solubility of surfactants in different phases that is due to the asymmetric parameter  $\alpha$ .

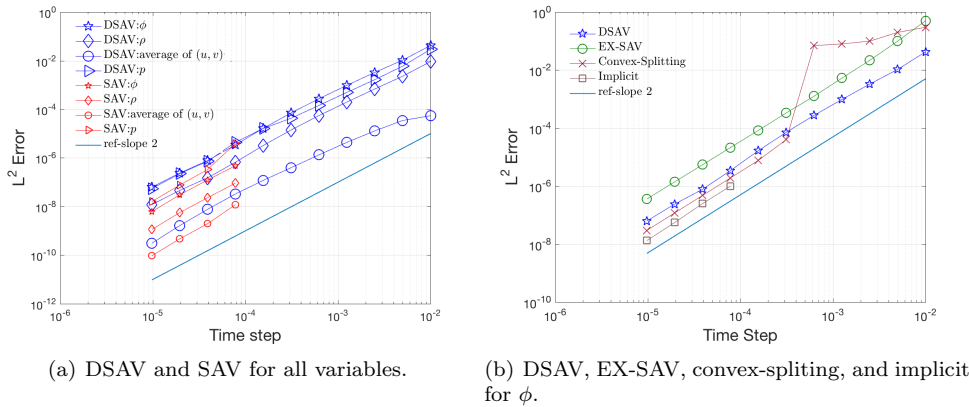


FIG. 3. Mesh refinement in time with the initial conditions given in (4.3), where (a) the  $L^2$  numerical errors of  $\phi$ ,  $\rho$ , the average of  $\mathbf{u} = (u, v)$ ,  $p$ , are calculated by DSAV (stabilized) and SAV (nonstabilized) with different time steps, and (b) the  $L^2$  numerical errors of  $\phi$  are calculated by using the schemes DSAV, EX-SAV, convex-splitting, and implicit.

More time refinement tests for temporal convergence are shown in Figure 3. Since the exact solutions are not known, we choose the numerical solutions computed by the scheme DSAV with a very tiny time step  $\delta t = 1e-9$  as the exact solution. The  $L^2$  errors of unknown variables at  $t = 0.5$  are computed by varying the time step  $\delta t$ . From the convergence rate shown in Figure 3(a) (which shows the errors of all variables), we find that the scheme DSAV always exhibits almost perfect second-order accuracy. However, when the nonstabilized scheme SAV uses a large time step, the convergence rate is very poor. Only for smaller time steps is the second-order accuracy displayed. In Figure 3(b), the errors for  $\phi$  computed by DSAV, EX-SAV, convex-splitting, and implicit are plotted, and their performances are similar to the previous accuracy test (hence the description is omitted here due to the page limit).

**4.1.3. Stability tests.** In this example, by plotting the temporal evolution of the free energy calculated by DSAV, we verify whether it is unconditional energy stable numerically. We still use the previous accuracy test on mesh refinement. In Figure 4, the evolution curves of the total free energy (3.64) computed using schemes DSAV and SAV are shown, respectively, where different time steps are used. In Figure 4(a), the evolution curves of the total free energy (3.64) calculated by DSAV are plotted, where we observe that monotonic attenuation is obtained, which confirms its unconditional energy stability.

For the nonstabilized scheme SAV, when  $\delta t > \frac{0.01}{2^{12}}$ , the computed energy blows up rapidly and only decays when using a smaller time step ( $\delta t \leq \frac{0.01}{2^{12}}$ ). Therefore, in Figure 4(b), we use the maximum time step ( $\delta t = \frac{0.01}{2^{12}}$ ) that SAV can take and also plot the energy curve computed by DSAV with a large time step ( $\delta t = \frac{0.01}{2^3}$ ) for comparison. The two energy curves are very consistent, which means that the time step of the DSAV scheme can be 512 times larger than the time step adopted by the nonstabilized scheme SAV for this test.

**4.2. Spinodal decomposition in two and three dimensions.** In this example, we use the developed scheme DSAV to study the phase separation dynamics (referred to as spinodal decomposition). We set the initial condition to be a homogeneous binary mixture, where a random number perturbation with a small magnitude

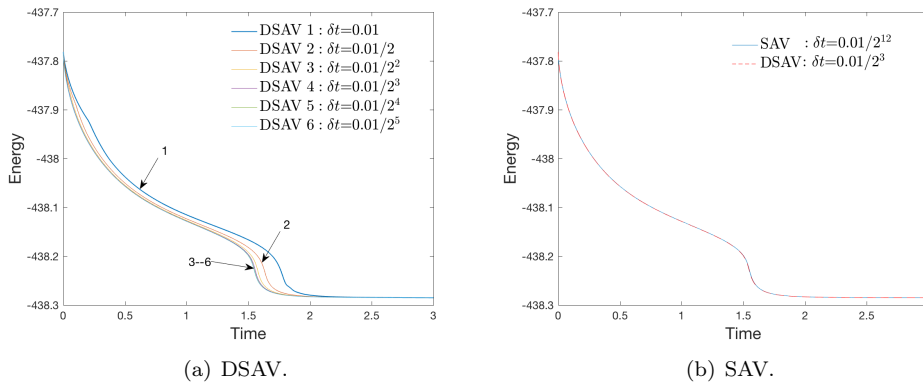


FIG. 4. Comparison of the total free energy (3.64) calculated by using schemes (a) DSAV and (b) SAV with different time steps.

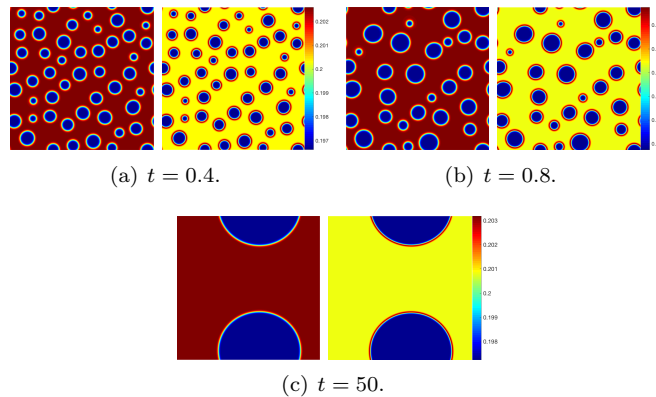


FIG. 5. 2D spinodal decomposition example, where snapshots of the profiles of  $\phi$  and  $\rho$  are plotted with  $t = 0.4, 0.8,$  and  $50$ . In each subfigure,  $\phi$  is on the left and  $\rho$  is on the right.

is applied to each grid point. Then, as time passes, the system develops from a homogeneous state caused by spontaneous increase to a two-phase state.

We first implement a 2D simulation where the initial conditions are given by

$$(4.4) \quad \mathbf{u}^0(\mathbf{x}) = 0, p^0(\mathbf{x}) = 0, \phi(\mathbf{x}) = 0.5 + 0.001\text{rand}(\mathbf{x}), \rho(\mathbf{x}) = 0.2,$$

where the  $\text{rand}(\mathbf{x})$  is the random number in  $[-1, 1]$  that follows the normal distribution. We assume periodic boundary conditions and set the computed domain to be  $[0, 2\pi]^2$ .  $257^2$  Fourier modes and time step  $1e-3$  are used for computations. The model parameters are set as  $M_1 = M_2 = 1, \lambda_1 = \lambda_2 = 0.01, \epsilon = 0.04, \eta = 0.01, \alpha = 1, \theta = 0.01, \zeta = 1e-5, \nu = 1, S_1 = S_2 = 0.1, B = 1e5$ . In Figure 5, the configuration profiles of  $\phi, \rho$  at different times are plotted. The final equilibrium solution appears to be circular, and the value of the concentration variable at the is significantly higher than at other locations.

We use the same initial conditions given in (4.4) to perform a 3D simulation. The computational domain is  $[0, 2]^3$  and discretized by using  $257^3$  Fourier modes. The time step is  $\delta t = 0.001$ , and order parameters are  $M_1 = M_2 = 1, \lambda_1 = \lambda_2 = 0.01, \epsilon =$

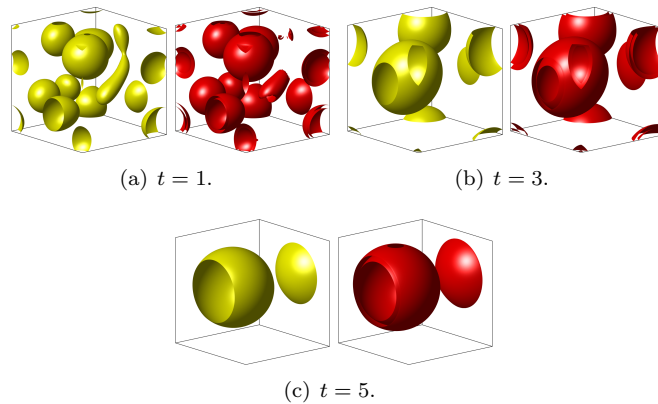
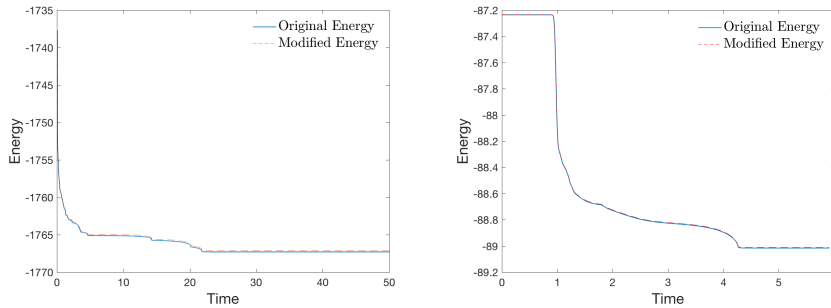


FIG. 6. 3D spinodal decomposition example, where snapshots of the isosurfaces of  $\{\phi = 0\}$  and  $\{\rho = 0.21\}$  (near the maximum value of  $\rho$ ) are plotted with  $t = 1, 3,$  and  $5$ . In each subfigure,  $\phi$  (yellow) is on the left and  $\rho$  (red) is on the right.



(a) Energy evolution for 2D spinodal decomposition. (b) Energy evolution for 3D spinodal decomposition.

FIG. 7. Comparison of the total free energy in the original form (2.2) and modified form (3.64) computed by using the scheme DSAV for the spinodal decomposition examples in two and three dimensions.

$0.06, \eta = 0.02, \alpha = 1, \theta = 0.01, \zeta = 1e-5, \nu = 1, S_1 = S_2 = 0.1, B = 1e5$ . In Figure 6, snapshots of the isosurfaces of  $\{\phi = 0\}$  and  $\{\rho = 0.21\}$  (near the maximum value of  $\rho$ ) are plotted. The dynamics of phase separation are similar to the 2D simulation, and the final steady state appears to be spherical. In Figure 7, we plot the time evolutions of the total free energy in the original form (2.2) and the modified form (3.64) and find that there is no viewable difference between them.

**4.3. Droplets coalescence/nonmergence phenomena with and without surfactant application under shear flow.** In this example, we study the effect of surfactants on the droplets deformation and coalescence dynamics driven by the imposed shear flow. We set the initial conditions to two adjacent circles (2D) and spheres (3D). Driven by the shear flow, the two droplets start to move in the opposite direction. If there is no surfactant, as time evolves, because the distance between the two droplets is very close, they will merge together due to coarsening effects. On the contrary, if the surfactant effect is added into the model, the droplets will slip away rather than merge, which implies the coarsening effect is overcome.

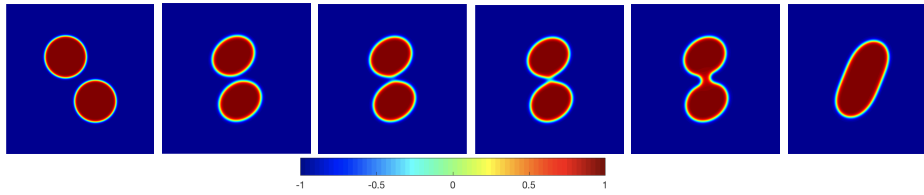


FIG. 8. The example of 2D droplet dynamics driven by shear flow without surfactant effect ( $\theta = \alpha = 0$ ). The snapshots of the configuration profiles of  $\phi$  are taken at  $t = 0, 1.5, 1.7, 1.75, 1.8,$  and  $3$ .

We first perform a 2D simulation with the computed domain  $\Omega = [0, 2]^2$ . The initial conditions read as follows:

$$(4.5) \quad \begin{aligned} \phi^0 &= \sum_{i=1}^2 \tanh \left( \frac{\sqrt{r_i - (x - x_i)^2 - (y - y_i)^2}}{\epsilon} \right) + 1, \\ \rho^0 &= 0.2, \mathbf{u}^0 = (0.35(y - 1), 0), p^0 = 0, \end{aligned}$$

where  $(x_1, y_1, r_1) = (0.8, 1.295, 0.28)$  and  $(x_2, y_2, r_2) = (1.2, 0.705, 0.28)$ . For the  $x$ -axis, we set periodic boundary conditions and use Fourier-spectral method to discretize it, where 513 Fourier modes are adopted. The boundary conditions for  $\mathbf{u} = (u, v)$ ,  $\phi$ , and  $\rho$  along the  $y$ -direction are set as follows:

$$(4.6) \quad u|_{(y=0,2)} = \pm 0.35, (v, \phi_y, \rho_y, \mu_y, \omega_y)|_{(y=0,2)} = 0.$$

The Legendre–Galerkin method is used to discretize the  $y$ -direction, where the Legendre polynomials with degrees up to 1024 are adopted. The model parameters for this simulation read as  $M_1 = M_2 = 0.01, \lambda_1 = \lambda_2 = 0.01, \epsilon = 0.02, \eta = 0.005, \zeta = 1e-5, \nu = 1, S_1 = S_2 = 0.1, B = 1e5, \delta t = 1e-3$ .

First, we set the coupling parameter  $\theta = 0, \alpha = 0$ , so the surfactant effect vanishes. In Figure 8, snapshots of the phase-field variable  $\phi$  at different times are plotted. We observe that the two droplets deform and move to each other under the action of shear flow. Around  $t = 1.75$ , they start to merge into a larger droplet by coarsening effects. Furthermore, we set the coupling parameter as  $\theta = 0.025, \alpha = 2$  and study how the drop motions are affected by surfactant effects. From Figure 9(a) and (b), which plots the configuration profiles of  $\phi$  and  $\rho$  at various times, we observe that surfactant prevents the fusion of droplets. This means that the action of surfactants can overcome the coarsening effect and completely change the way the droplets move. Similar dynamics were observed experimentally in [24, 36, 66], and some simulations in two dimensions were performed using alternative phase-field surfactant models in [35].

We continue to perform 3D simulations. The computed domain is set as  $(x, y, z) \in \Omega = [0, 2] \times [0, 0.7] \times [0, 0.2]$ , and the initial conditions read as (shown in the first subfigure of Figure 10)

$$(4.7) \quad \begin{aligned} \phi^0 &= \sum_{i=1}^2 \tanh \left( \frac{\sqrt{r_i - (x - x_i)^2 - (y - y_i)^2 - (z - z_i)^2}}{\epsilon} \right) + 1, \rho^0 = 0.2, \\ \mathbf{u}^0 &= (0.7(y - 1), 0, 0), p^0 = 0, \end{aligned}$$

where  $(x_1, y_1, z_1, r_1) = (0.8, 0.35, 1.272, 0.28)$  and  $(x_2, y_2, z_2, r_2) = (1.2, 0.35, 0.728, 0.28)$ . Periodic boundary conditions are assumed for the  $x$  and  $y$ -directions. We discretize

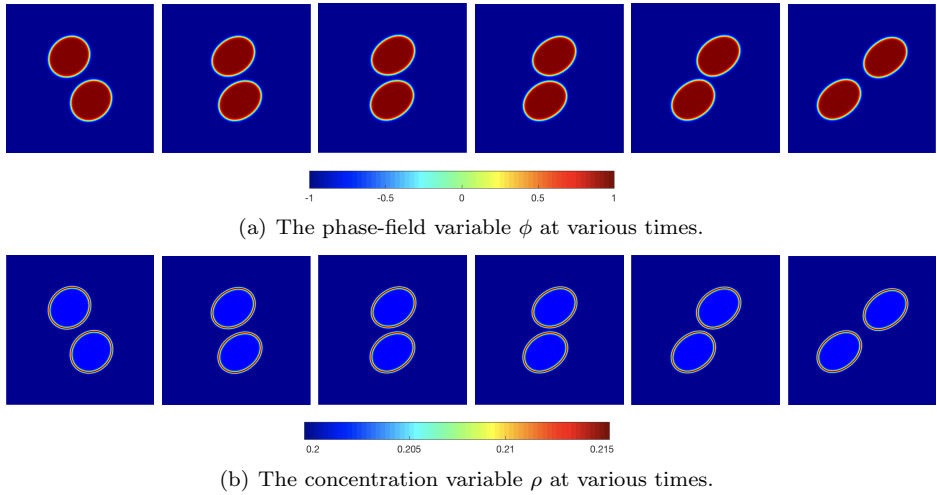


FIG. 9. The example of 2D droplet dynamics driven by shear flow with surfactant effect ( $\theta = 0.025, \alpha = 2$ ). The snapshots of the configuration profiles of  $\phi$  are taken at  $t = 0.5, 1.5, 2, 2.5, 3.5,$  and  $5$ .

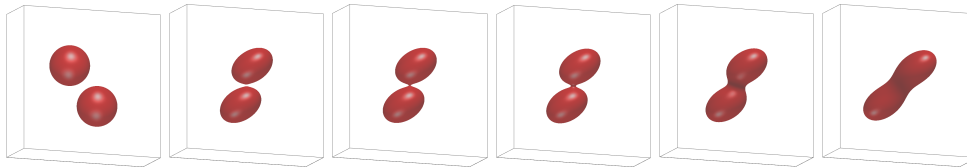


FIG. 10. 3D droplet deformation dynamics driven by the shear flow without surfactant effect ( $\theta = \alpha = 0$ ). Snapshots of the isosurfaces  $\{\phi = 0\}$  (red) are taken at  $t = 0, 1.65, 1.675, 1.7, 2,$  and  $2.5$ .

them by using  $257^2$  Fourier-modes. The boundary conditions along the  $z$ -direction for variables  $\mathbf{u} = (u, v, w), \phi, \rho, \mu, \omega$  read as

$$(4.8) \quad u|_{(z=0,2)} = \pm 0.7, (v, w, \phi_z, \rho_z, \mu_z, \omega_z)|_{(z=0,2)} = 0.$$

The spatial discretization for the  $z$ -direction is based on the Legendre–Galerkin method, and the Legendre polynomials with degrees up to 256 are used. The order parameters are the same as the 2D simulations. In Figure 10, we plot the isosurfaces of  $\{\phi = 0\}$  for the case of no surfactant where the coupling parameters are set as  $\theta = 0, \alpha = 0$ . The two droplets move, deform, and then merge into a larger droplet due to the coarsening effect. With the surfactant effect ( $\theta = 0.02, \alpha = 1$ ), the two droplets slide and finally depart from each other, as shown in Figure 11, where isosurfaces of  $\{\phi = 0\}$  (red) and  $\{\rho = 0.21\}$  (yellow) are plotted.

**5. Concluding remarks.** To solve a challenging, hydrodynamically coupled Cahn–Hilliard phase-field binary surfactant model, we have designed a novel time marching scheme that can include almost all the desired characteristics: linear, second-order accurate in time, fully decoupled, and unconditionally energy stable. The novelty of the scheme is the development of a novel, universally applicable decoupling method. Its key idea is based on a well-known but often ignored zero-energy-contribution property satisfied by the coupled nonlinear terms between the flow-field

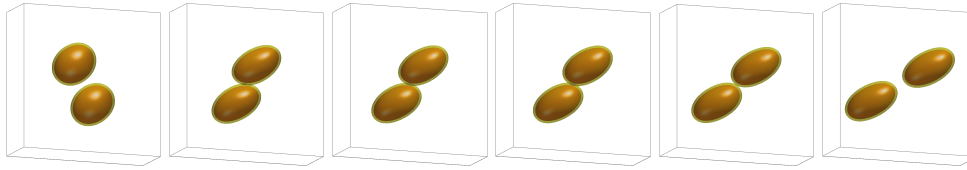


FIG. 11. 3D droplet deformation dynamics driven by the shear flow with surfactant effect ( $\theta = 0.02$ ,  $\alpha = 1$ ). Snapshots of the isosurfaces  $\{\phi = 0\}$  (red) and  $\{\rho = 0.21\}$  (yellow) are taken at  $t = 0.5, 2, 2.25, 2.3, 2.75, \text{ and } 3.5$ .

and phase-field variables. We give a detailed practical implementation and also prove the unconditional energy stability rigorously. By simulating a large number of 2D and 3D numerical examples and comparing them with several other popular methods, we numerically prove the effectiveness of the developed scheme. To the best of the author's knowledge, the developed scheme is the first one that owns the fully decoupled nature and second-order accurate in time for the hydrodynamics coupled phase-field surfactant model.

#### REFERENCES

- [1] R. BACKOFEN, S. M. WISE, M. SALVALAGLIO, AND A. VOIGT, *Convexity splitting in a phase field model for surface diffusion*, Int. J. Numer. Anal. Model., 16 (2019), pp. 192–209.
- [2] C. CHEN AND X. YANG, *Efficient numerical scheme for a dendritic solidification phase field model with melt convection*, J. Comput. Phys., 388 (2019), pp. 41–62.
- [3] C. CHEN AND X. YANG, *Fast, provably unconditionally energy stable, and second-order accurate algorithms for the anisotropic Cahn-Hilliard model*, Comput. Methods Appl. Mech. Engrg., 351 (2019), pp. 35–59.
- [4] M. I. M. COPETTI AND C. M. ELLIOTT, *Numerical analysis of the Cahn-Hilliard equation with a logarithmic free energy*, Numer. Math., 63 (1992), pp. 39–65.
- [5] Q. DU AND R. A. NICOLAIDES, *Numerical analysis of a continuum model of phase transition*, SIAM J. Numer. Anal., 28 (1991), pp. 1310–1322.
- [6] C. M. ELLIOTT AND H. GARCKE, *On the Cahn-Hilliard equation with degenerate mobility*, SIAM J. Math. Anal., 27 (1996), pp. 404–423.
- [7] D. J. EYRE, *Unconditionally gradient stable time marching the Cahn-Hilliard equation*, in Proceedings of Computational and Mathematical Models of Microstructural Evolution, Mater. Res. Soc. Sympos. Proc. 529, MRS, Warrendale, PA, 1998, pp. 39–46.
- [8] X. FENG, *Fully discrete finite element approximations of the Navier-Stokes-Cahn-Hilliard diffuse interface model for two-phase fluid flows*, SIAM J. Numer. Anal., 44 (2006), pp. 1049–1072.
- [9] I. FONSECA, M. MORINI, AND V. SLASTIKOV, *Surfactants in foam stability: A phase-field approach*, Arch. Ration. Mech. Anal., 183 (2007), pp. 411–456.
- [10] K. GLASNER AND S. ORIZAGA, *Improving the accuracy of convexity splitting methods for gradient flow equations*, Math. Comp., 315 (2016), pp. 52–64.
- [11] H. GOMEZ, V. M. CALO, Y. BAZILEVS, AND T. J. R. HUGHES, *Isogeometric analysis of the Cahn-Hilliard phase-field model*, Comput. Methods Appl. Mech. Engrg., 197 (2008), pp. 4333–4352.
- [12] H. GOMEZ, DER ZEE VAN, AND G. KRISTOFFER, *Computational phase-field modeling*, in Encyclopedia of Computational Mechanics, 2nd ed., John Wiley & Sons, New York, 2017.
- [13] H. GOMEZ AND X. NOGUEIRA, *A new space-time discretization for the Swift-Hohenberg equation that strictly respects the Lyapunov functional*, Commun. Nonlinear Sci. Numer. Simul., 17 (2012), pp. 4930–4946.
- [14] G. GOMPPER AND M. SCHICK, *Self-assembling amphiphilic systems*, in Phase Transitions and Critical Phenomena, C. Domb and J. Lebowitz, eds., Academic Press, London, 1994.
- [15] Y. GONG, J. ZHAO, AND Q. WANG, *Second order fully discrete energy stable methods on staggered grids for hydrodynamic phase field models of binary viscous fluids*, SIAM J. Sci. Comput., 40 (2018), pp. B528–B553.
- [16] J. L. GUERMOND, P. MINEV, AND J. SHEN, *An overview of projection methods for incompressible flows*, Comput. Methods Appl. Mech. Engrg., 195 (2006), pp. 6011–6045.

- [17] J. L. GUERMOND AND L. QUARTAPELLE, *A projection FEM for variable density incompressible flows*, J. Comput. Phys., 165 (2000), pp. 167–188.
- [18] J. L. GUERMOND AND A. SALGADO, *A splitting method for incompressible flows with variable density based on a pressure Poisson equation*, J. Comput. Phys., 228 (2009), pp. 2834–2846.
- [19] J. L. GUERMOND AND J. SHEN, *On the error estimates of rotational pressure-correction projection methods*, Math. Comp., 73 (2004), pp. 1719–1737.
- [20] F. GUILLEN-GONZALEZ AND G. TIERRA, *Unconditionally energy stable numerical schemes for phase-field vesicle membrane model*, J. Comput. Phys., 354 (2018), pp. 67–85.
- [21] Z. GUO, P. LIN, AND J. S. LOWENGRUB, *A numerical method for the quasi-incompressible Cahn–Hilliard–Navier–Stokes equations for variable density flows with a discrete energy law*, J. Comput. Phys., 276 (2014), pp. 486–507.
- [22] D. HAN, A. BRYLEV, X. YANG, AND Z. TAN, *Numerical analysis of second order, fully discrete energy stable schemes for phase field models of two phase incompressible flows*, J. Sci. Comput., 70 (2017), pp. 965–989.
- [23] D. HAN AND X. WANG, *A second order in time, uniquely solvable, unconditionally stable numerical scheme for Cahn–Hilliard–Navier–Stokes equation*, J. Comput. Phys., 290 (2015), pp. 139–156.
- [24] Y. T. HU, D. J. PINE, AND L. G. LEAL, *Drop deformation, breakup, and coalescence with compatibilizer*, Phys. Fluids., 3 (2000), pp. 484–489.
- [25] L. JU, X. LI, Z. QIAO, AND H. ZHANG, *Energy stability and error estimates of exponential time differencing schemes for the epitaxial growth model without slope selection*, Math. Comp., 87 (2018), pp. 1859–1885.
- [26] D. KAY, V. STYLES, AND R. WELFORD, *Finite element approximation of a Cahn–Hilliard–Navier–Stokes system*, Interfaces Free Bound., 10 (2008), pp. 15–43.
- [27] J. KIM, *Numerical simulations of phase separation dynamics in a water-oil-surfactant system*, J. Colloid Interface Sci., 303 (2006), pp. 272–279.
- [28] S. KOMURA AND H. KODAMA, *Two-order-parameter model for an oil-water-surfactant system*, Phys. Rev. E., 55 (1997), pp. 1722–1727.
- [29] M. LARADJI, H. GUO, M. GRANT, AND M. J. ZUCKERMANN, *The effect of surfactants on the dynamics of phase separation*, J. Phys. Condensed Matter, 4 (1992), 6715.
- [30] M. LARADJI, O. G. MOURISTEN, S. TOXVAERD, AND M. J. ZUCKERMANN, *Molecular dynamics simulations of phase separation in the presence of surfactants*, Phys. Rev. E., 50 (1994), pp. 1722–1727.
- [31] X. LI, J. SHEN, AND Z. LIU, *New SAV-Pressure Correction Methods for the Navier-Stokes Equations: Stability and Error Analysis*, arXiv:2002.09090, 2020.
- [32] L. LIN, Z. YANG, AND S. DONG, *Numerical approximation of incompressible Navier-Stokes equations based on an auxiliary energy variable*, J. Comput. Phys., 388 (2019), pp. 1–22.
- [33] P. LIN, C. LIU, AND H. ZHANG, *An energy law preserving CO finite element scheme for simulating the kinematic effects in liquid crystal flow dynamics*, J. Comput. Phys., 227 (2007), pp. 1411–1427.
- [34] C. LIU, J. SHEN, AND X. YANG, *Decoupled energy stable schemes for a phase-field model of two-phase incompressible flows with variable density*, J. Sci. Comput., 62 (2015), pp. 601–622.
- [35] H. LIU AND Y. ZHANG, *Phase-field modeling droplet dynamics with soluble surfactants*, J. Comput. Phys., 229 (2010), pp. 9166–9187.
- [36] S. LYU, T. D. JONES, F. S. BATES, AND C. W. MACOSKO, *Role of block copolymers on suppression of droplet coalescence*, Macromolecules, 35 (2002), pp. 7845–7855.
- [37] Y. MA, *Wetting-driven structure formation of a binary mixture in the presence of a mobile particle pinning potential*, Phys. Rev. E., 62 (2000), 8207.
- [38] S. MINJEAUD, *An unconditionally stable uncoupled scheme for a triphasic Cahn–Hilliard/Navier–Stokes model*, Numer. Methods Partial Differential Equations, 29 (2013), pp. 584–618.
- [39] R. NOCHETTO AND J.-H. PYO, *The gauge-Uzawa finite element method part I: The Navier–Stokes equations*, SIAM J. Numer. Anal., 43 (2005), pp. 1043–1068.
- [40] R. RANNACHER, *On Chorin’s projection method for the incompressible Navier–Stokes equations*, in the Navier–Stokes Equations II, Lecture Notes in Math. 1530, Springer, New York, 1991.
- [41] J.-R. ROAN AND E. I. SHAKHNOVICH, *Phase separation of a binary fluid containing surfactants in a Hele–Shaw cell*, Phys. Rev. E., 59 (1999), p. 2109.
- [42] I. ROMERO, *Thermodynamically consistent time stepping algorithms for nonlinear thermomechanical systems*, Internat. J. Numer. Methods Engrg., 79 (2009), pp. 706–732.
- [43] C. WANG S. M. WISE AND J. S. LOWENGRUB, *An energy-stable and convergent finite-difference scheme for the phase field crystal equation*, SIAM J. Numer. Anal., 47 (2009), pp. 2269–2288.

- [44] A. F. SARMIENTO, L. F. R. ESPATH, P. VIGNAL, L. DALCIN, M. PARSANI, AND V. M. CALO, *An energy-stable generalized- $\alpha$  method for the Swift–Hohenberg equation*, J. Comput. Appl. Math., 344 (2018), pp. 836–851.
- [45] J. SHEN, C. WANG, S. WANG, AND X. WANG, *Second-order convex splitting schemes for gradient flows with Ehrlich–Schwoebel type energy: Application to thin film epitaxy*, SIAM J. Numer. Anal., 50 (2012), pp. 105–125.
- [46] J. SHEN, J. XU, AND J. YANG, *A new class of efficient and robust energy stable schemes for gradient flows*, SIAM Rev., 61 (2019), pp. 474–506.
- [47] J. SHEN, J. XUE, AND J. YANG, *The scalar auxiliary variable (SAV) approach for gradient flows*, J. Comput. Phys., 353 (2018), pp. 407–416.
- [48] J. SHEN AND X. YANG, *Numerical approximations of Allen–Cahn and Cahn–Hilliard equations*, Discrete Contin. Dyn. Syst., 28 (2010), pp. 1669–1691.
- [49] J. SHEN AND X. YANG, *A phase-field model and its numerical approximation for two-phase incompressible flows with different densities and viscosities*, SIAM J. Sci. Comput., 32 (2010), pp. 1159–1179.
- [50] J. SHEN AND X. YANG, *Decoupled energy stable schemes for phase field models of two phase complex fluids*, SIAM J. Sci. Comput., 36 (2014), pp. B122–B145.
- [51] J. SHEN AND X. YANG, *Decoupled, energy stable schemes for phase-field models of two-phase incompressible flows*, SIAM J. Numer. Anal., 53 (2015), pp. 279–296.
- [52] J. SHEN AND X. YANG, *The IEQ and SAV approaches and their extensions for a class of highly nonlinear gradient flow systems*, Contemp. Math., 754 (2020), pp. 217–245.
- [53] J. SHEN, X. YANG, AND H. YU, *Efficient energy stable numerical schemes for a phase field moving contact line model*, J. Comput. Phys., 284 (2015), pp. 617–630.
- [54] T. TANG, *On effective numerical methods for phase-field models*, Proc. Int. Cong. of Math., 4 (2018), pp. 3687–3708.
- [55] C. H. TENG, I. L. CHERN, AND M. C. LAI, *Simulating binary fluid-surfactant dynamics by a phase field model*, Discrete Contin. Dyn. Syst., 17 (2010), pp. 1289–1307.
- [56] T. TERAMOTO AND F. YONEZAWA, *Droplet growth dynamics in a water-oil-surfactant system*, J. Colloid Inter. Sci., 235 (2001), pp. 329–333.
- [57] R. VAN DER SMAN AND S. VAN DER GRAAF, *Diffuse interface model of surfactant adsorption onto flat and droplet interfaces*, Rheol. Acta, 46 (2006), pp. 3–11.
- [58] R. G. M. VAN DER SMAN AND M. B. J. MEINDERS, *Analysis of improved lattice Boltzmann phase field method for soluble surfactants*, Comput. Phys. Commun., 199 (2016), pp. 12–21.
- [59] J. XU, Y. LI, S. WU, AND A. BOUSQUET, *On the stability and accuracy of partially and fully implicit schemes for phase field modeling*, Comput. Methods Appl. Mech. Engrg., 345 (2019), pp. 826–853.
- [60] X. YANG, *Linear, first and second order and unconditionally energy stable numerical schemes for the phase field model of homopolymer blends*, J. Comput. Phys., 327 (2016), pp. 294–316.
- [61] X. YANG, *Numerical approximations for the Cahn–Hilliard phase field model of the binary fluid-surfactant system*, J. Sci. Comput., 74 (2017), pp. 1533–1553.
- [62] X. YANG AND L. JU, *Linear and unconditionally energy stable schemes for the binary fluid-surfactant phase field model*, Comput. Methods Appl. Mech. Engrg., 318 (2017), pp. 1005–1029.
- [63] X. YANG AND H. YU, *Efficient second order unconditionally stable schemes for a phase field moving contact line model using an invariant energy quadratization approach*, SIAM J. Sci. Comput., 40 (2018), pp. B889–B914.
- [64] X. YANG, J. ZHAO, Q. WANG, AND J. SHEN, *Numerical approximations for a three components Cahn–Hilliard phase-field model based on the invariant energy quadratization method*, Math. Model Methods Appl. Sci., 27 (2017), pp. 1993–2030.
- [65] Z. YANG AND S. DONG, *An unconditionally energy-stable scheme based on an implicit auxiliary energy variable for incompressible two-phase flows with different densities involving only precomputable coefficient matrices*, J. Comput. Phys., 393 (2018), pp. 229–257.
- [66] Y. YOON, A. HSU, AND L. LEAL, *Experimental investigation of the effects of copolymer surfactants on flow-induced coalescence of drops*, Phys. Fluids, 19 (2007), 023102.
- [67] H. YU AND X. YANG, *Numerical approximations for a phase-field moving contact line model with variable densities and viscosities*, J. Comput. Phys., 334 (2017), pp. 665–686.
- [68] C. WANG, Z. HU, S. M. WISE, AND J. S. LOWENGRUB, *Stable and efficient finite difference nonlinear-multigrid schemes for the phase field crystal equation*, J. Comput. Phys., 228 (2009), pp. 5323–5339.

- [69] J. ZHANG, C. CHEN, J. WANG, AND X. YANG, *Efficient, second order accurate, and unconditionally energy stable numerical scheme for a new hydrodynamics coupled binary phase-field surfactant system*, *Comput. Phys. Commun.*, 251 (2020), 107122.
- [70] J. ZHANG AND X. YANG, *Decoupled, non-iterative, and unconditionally energy stable large time stepping method for the three-phase Cahn-Hilliard phase-field model*, *J. Comput. Phys.*, 404 (2020), 109115.
- [71] G. ZHU, J. KOU, S. SUN, J. YAO, AND A. LI, *Decoupled, energy stable schemes for a phase-field surfactant model*, *Comput. Phys. Commun.*, 233 (2018), pp. 67–77.